

1
2
3
4
5
6
7
8
9
10
11
12
13
14
15
16
17
18
19
20
21
22
23
24
25
26
27
28
29

Convective hydration in the tropical tropopause layer during the StratoClim aircraft campaign:
Pathway of an observed hydration patch

Keun-Ok Lee¹, Thibaut Dauhut¹, Jean-Pierre Chaboureau¹, Sergey Khaykin², Martina Krämer³ and
Christian Rolf³

¹Laboratoire d'Aérodologie, Université de Toulouse, CNRS, UPS, Toulouse, France

²LATMOS-IPSL, Université Versailles St-Quentin; Sorbonne Université, CNRS/INSU, Guyancourt, France

³Institute for Energy and Climate Research – Stratosphere (IEK-7), Forschungszentrum Jülich, Jülich, Germany

ABSTRACT

The source and pathway of the hydration patch in the TTL (Tropical Tropopause Layer) that was measured during the StratoClim field campaign during the Asian summer monsoon in 2017, and its connection to convective overshoots are investigated. During flight #7, two remarkable layers are measured in the TTL namely, (1) moist layer (ML) with water vapour content of 4.8–5.7 ppmv in altitudes of 18–19 km altitudes in the lower stratosphere, and (2) ice layer (IL) with ice content up to 1.9 eq. ppmv in altitudes of 17–18 km in the upper troposphere around 06:30 UTC on 8 August to the south of Kathmandu (Nepal). A Meso-NH convection-permitting simulation succeeds in reproducing the characteristics of ML and IL. Through analysis, we show that ML and IL are generated by convective overshoots that occurred over the Sichuan basin about 1.5 day before. Overshooting clouds develop up to 19 km, hydrating the lower stratosphere of up to 20 km with 6401 t of water vapour by a strong-to-moderate mixing of the updraughts with the stratospheric air. A few hours after the initial overshooting phase, a hydration patch is generated, and a large amount of water vapour (above 18 ppmv) remained at even higher altitudes up to 20.5 km while the anvil cloud top descends to 18.5 km. At the same time, a great part of the hydrometeors falls shortly, and the water vapour concentration in ML and IL decreases due to turbulent diffusion by mixing with the tropospheric air, ice nucleation, and water vapour deposition. As the hydration patch continues to travel toward the south of Kathmandu, tropospheric tracer concentration increases up to ~30 and 70 % in ML and IL, respectively. The air mass in the layers becomes gradually diffused and it has less and less water vapour and ice content by mixing with the dry tropospheric air.

30

31

32 **1. Introduction**

33 The Asian summer monsoon anticyclone is one of the most pronounced circulation patterns in the Northern
34 Hemisphere, and it is a dominant climatological feature of the global circulation during boreal summer
35 (Mason and Anderson, 1963; Randel and Park, 2006). The monsoon circulation horizontally covers large
36 parts of southern Asia and the Middle East, and is located on the edge of the tropics and subtropics. It
37 consists of cyclonic flow and convergence in the lower troposphere together with strong anticyclonic
38 circulation and divergence in the upper troposphere. This circulation is coupled with persistent deep
39 convection over the south Asia region during summer (June to September) (Hoskins and Rodwell, 1995).
40 The monsoon tropopause is relatively high at about 4.2 ppmv; the upper tropospheric anticyclonic circulation
41 extends into the lower stratosphere spanning from around 300 hPa and 70 hPa, i.e. approximately the whole
42 upper troposphere and lower stratosphere (UTLS) (Highwood and Hoskins, 1998; Randel and Park, 2006).

43 Due to the strong dynamical signature in the UTLS, the influence of the monsoon is evident in
44 chemical constituents, i.e. water vapour is relatively high at about 4.2 ppmv (Wright et al., 2011), ozone is
45 relatively low (Randel et al., 2001), and methane, nitrogen oxides, and carbon monoxide are relatively high
46 (Park et al., 2004; Liu et al., 2005). Especially, the water vapour in the UTLS is controlled by the
47 troposphere-to-stratosphere transport of moisture across the tropical tropopause layer (TTL, located between
48 ~150 hPa (355 K, 14 km) and ~70 hPa (425 K, 18.5 km); Fueglistaler et al., 2009; Rolf et al., 2018). It is
49 mainly driven by the large-scale cold point tropopause temperature field, but also processes involving
50 convection, gravity waves, and cirrus cloud microphysics that modulate TTL humidity.

51 Convective overshoots that penetrate the tropopause directly inject air and water into the stratosphere.
52 Fundamentally, convection arises from the temperature difference between a parcel of warm air and the
53 cooler air surrounding it. Warm air, which is less dense, i.e. more buoyant, rises through the atmospheric
54 column and adiabatically expands and cools. When the temperature of the rising air parcel has cooled
55 sufficiently, the water vapour it contains will begin to condense and release latent heat. If air parcels within
56 the convective core have enough upward momentum, they continue to rise beyond their equilibrium level of
57 zero buoyancy, and form overshoots. They eventually form an overshoot that penetrate into the lowermost
58 stratosphere by crossing the cold point tropopause. The convective overshoots have the potential to increase

59 the humidity in the stratosphere via rapid sublimation of convectively lofted ice and mixing with dry
60 stratospheric air. This has been demonstrated in previous studies in both modelling and measurement
61 (Dessler and Sherwood, 2004; Chaboureau et al., 2007; Jensen et al., 2007; Homeyer et al., 2014; Khaykin
62 et al., 2016; Rysman et al., 2016; Homeyer et al., 2017; Smith et al., 2017; Dauhut et al., 2018; Funatsu et al.,
63 2018; among others). Even a small volume of tropospheric air can carry a significant quantity of water in the
64 condensed phase. Mixing of tropospheric air with the surrounding stratosphere, which is typically sub-
65 saturated, facilitates the rapid sublimation of lofted ice. Also, the origin of the injected water to the TTL has
66 been studied by backward trajectory analysis at global scale, and it was found that the convective sources are
67 generally higher over the continental part of the Asian monsoon region in comparison to other tropical
68 regions, with shorter transit times (Tzella and Legras, 2005; Tissier and Legras, 2016). However, the net
69 contribution of convective overshoots to stratospheric water vapour concentration is not well understood at
70 mesoscale and is not well represented in global models because of the small spatial scales (less than a few
71 kilometres) and short time scales (less than few hours) over which convection occurs.

72 The tropical aircraft campaign of the Stratospheric and upper tropospheric processes for better Climate
73 predictions (StratoClim, www.stratoclim.org) took place in summer 2017. It aimed to improve our
74 knowledge of the key processes, i.e. microphysical, chemical and dynamical processes, which determine the
75 composition of the UTLS, such as the formation, loss, and redistribution of chemical constituents (water
76 vapour, ozone, and aerosol). During the campaign, eight dedicated flights were successfully operated with
77 the objective of documenting the connection between the moisture plumes in the UTLS and the convective
78 sources from south Kathmandu, Nepal, during summer monsoon season.

79 Our study focuses on part of flight #7 to the south of Kathmandu measuring the stratospheric
80 hydration in the altitudes between 17 and 19 km. The objective of our work is to investigate the source and
81 pathway of the localized moisture in the TTL that was measured by aircraft in connection to a convective
82 overshoot. This is done using a combination of airborne and spaceborne observations as well as a
83 convection-permitting simulation performed with a fine resolution in the TTL.

84 A detailed description of the dataset is given in section 2. Section 3 presents the moistened TTL
85 signature captured by airborne and spaceborne observations and the numerical simulation. Section 4
86 demonstrates the convective origin of the enhanced moisture and shows its evolution along its path in the
87 lower stratosphere. A summary and discussion of the findings of the present study are given in section 5.

88

89

90 **2. Data and method**

91 M55-Geophysica aircraft deployment in Kathmandu during Asian Summer Monsoon in July-August 2017
92 provided unprecedented sampling of the UTLS region above the southern slopes of Himalayas. More details
93 concerning the observational datasets used in this study together with the airborne and spaceborne
94 measurements and the convection-permitting simulation are provided in the following.

95

96 *2.1. StratoClim airborne observations*

97 During flight #7, the M55-Geophysica aircraft flew back and forth between Kathmandu in Nepal and west
98 Bengal in India (for the track, see the red line in Fig. 1) from 04:30 UTC to 06:50 UTC on 8 August 2017.
99 In-situ sensor onboard the aircraft measures the relative humidity with respect to ice (hereafter called simply
100 ‘relative humidity’ or ‘RH_{ice}’), temperature and wind speed and direction every 1 second. FLASH and FISH
101 instruments on board the Geophysica aircraft sampled the vertical water vapour and ice content distribution
102 every 1 second, respectively.

103 FLASH-A (Fluorescent Lyman-Alpha Stratospheric Hygrometer for Aircraft) is an advanced version
104 of the airborne FLASH instrument (Sitnikov et al, 2007; Khaykin et al., 2013) previously flown onboard the
105 M55-Geophysica aircraft. FLASH-A has a rear facing inlet allowing measurement of gas-phase water in the
106 altitude range between 12–21 km, with the latter being the aircraft ceiling altitude. Total uncertainty of water
107 vapour measurement amounts to 9 % with a detection limit of 0.2 ppmv, whereas the measurement precision
108 at 1 Hz sampling is better than 6 %.

109 FISH (Fast In situ Stratospheric Hygrometer) is a closed-path Lyman- α photo fragment fluorescence
110 hygrometer that measures total water (sum of gas phase and evaporated ice crystals) in the range of 1–1000
111 ppmv between 50 and 500 hPa levels with an accuracy and precision of 6–8 % and 0.3 ppmv (Zöger et al.,
112 1999; Meyer et al., 2015). The time resolution of the measurements is 1 Hz. Inside of ice clouds, ice water
113 content (IWC) is calculated by subtracting the gas phase water measured by FLASH from the total water
114 detected by FISH as described by Afchine et al. (2018). The minimum detectable IWC is 3×10^{-2} ppmv
115 ($\sim 3 \times 10^{-3}$ mg m⁻³).

116

117 2.2. Spaceborne observation

118 Calibrated thermal infrared brightness temperature (BT) data at 10.8 μm wavelength, acquired every 15 min
119 by the Spinning Enhanced Visible and Infrared Imager (SEVIRI) onboard the geostationary Meteosat Second
120 Generation satellite (MSG) were employed to investigate the evolution of deep convection. The spatial
121 resolution of the MSG-SEVIRI data used is 0.05° in both latitude and longitude. BT minima are generally
122 indicative of the cloud top overshoots associated with deep convection (e.g. Kato, 2006, Lee et al., 2016).

123 Vertical profiles of backscatter retrieved from the Cloud-Aerosol Lidar with Orthogonal Polarization
124 (CALIOP) on board CALIPSO (Winker et al. 2009) with a wavelength at 532 nm are used. CALIOP
125 provides observations of particles, including high clouds, with a very high sampling resolution, 30 and 335 m
126 in the vertical and horizontal directions, respectively.

127

128 2.3. Cloud-resolving numerical simulation

129 The target convective overshoots and the moistened TTL were simulated using the non-hydrostatic numerical
130 research model, Meso-NH (Lac et al. 2018). For a fine-scale analysis, the simulation uses about 400 million
131 grid points with horizontal grid spacing of 2.5 km. The vertical grid has 144 stretched levels (Gal-Chen and
132 Somerville, 1975) with a spacing of 250 m in the free troposphere and the stratosphere and a finer resolution
133 of 100 m close to the surface and between 16 and 19.5 km inside the TTL. The simulation domain covers
134 northern India and China (Fig. 1, 5000 km \times 3600 km) encompassing the track of flight #7 and the
135 overshooting clouds over the Sichuan basin. The simulation was initialized at 00:00 UTC on 6 August 2017
136 and the initial and lateral boundary conditions are provided by the operational European Centre for Medium-
137 Range Weather Forecasts (ECMWF) analyses every 6 hours. It ran for 3 days providing outputs every 1 hour.

138 The model employs a 1-moment bulk microphysical scheme (Pinty and Jabouille, 1998), which
139 governs the equations of six water categories (water vapour, cloud water, rainwater, pristine ice, snow and
140 graupel). For each particle type, the sizes follow a generalized Gamma distribution while power-law
141 relationships allow the mass and fall speed to be linked to the diameters. Except for cloud droplets, each
142 condensed water species has a nonzero fall speed. The turbulence parametrisation is based on a 1.5-order
143 closure (Cuxart et al., 2000) of the turbulent kinetic energy equation and uses the Bougeault and Lacarrere
144 (1989) mixing length. The transport scheme for momentum variables is the weighted essentially non-
145 oscillatory (WENO) scheme of 5th order (Shu and Osher, 1988) while other variables are transported with the

146 piecewise parabolic method (PPM) scheme (Colella and Woodward, 1984), a scheme with excellent mass-
147 conservation properties and low numerical diffusion (Muller, 1992).

148 To assess the simulation, airborne measurement data (along about 85.2°E, 25–26.5°N, blue line in Fig.
149 1) between 06:20 and 06:48 UTC on 8 August 2017 are compared to the simulation results averaged in a box
150 (85–85.5°E, 25–26.5°N, marked by ‘HYD’ in Fig. 1) at 06:00 UTC on the same day. The CALIOP
151 backscatter coefficients are compared to those simulated from the model outputs using the Meso-NH lidar
152 simulator, which takes into account all the predicted scattering particles (Chaboureau et al. 2011). The
153 SEVIRI/MSG BTs are compared to synthetic BTs computed offline using the Radiative Transfer for TIROS
154 Operational Vertical Sounder (RTTOV) code version 11.3 (Saunders et al. 2013) from the simulation outputs
155 (Chaboureau et al. 2008).

156 In this study, a ‘hydration patch’ is defined as a region with a water vapour amount larger than the
157 background value at 410 K isentropic level. The background equals 5.2 ppmv which corresponds to the water
158 vapour averaged in the box 74–84°E, 15–25°N (shown with dashed line in Fig. 1). Such a hydration patch is
159 located within the moist layer (ML) of 18–19 km altitude (see Figure 2), corresponding to an enhanced value
160 of water vapour observed during the last descending of flight #7 (see section 3.1). Below the hydration patch,
161 the ice layer (IL) is located between 17 and 18 km, where an increase of ice content is observed during the
162 same period. The hydration patch is chased visually back in time every hour from 06:00 UTC on 8 August to
163 13:00 UTC on 6 August 2017 (for more details, see Figure S1 in the Supplement), considering the prevailing
164 wind direction and speed at 410 K isentropic altitude. At 14:00 UTC, a large amount of water vapour (≥ 6.6
165 ppmv), that is injected by the convective overshoot in the Sichuan basin, starts to appear at this altitude,
166 generating a hydration patch. With the dominant north-easterlies ($15\text{--}20\text{ m s}^{-1}$), it travels to the south of
167 Kathmandu. The area of the hydration patch is about 6,000 km², but it is reduced to one fourth to about 1,500
168 km² during the initial overshooting phase in the convective region. This domain is used to calculate the
169 average values of water vapour, ice content, temperature, and relative humidity displayed in Figures 9, 10,
170 and 11.

171 To understand the processes along the pathway of the hydration patch, four analysis times are selected:
172 1) a few hours before the overshoot development at 13:00 UTC on 6 August, 2) the overshoot development
173 time at 21:00 UTC on the same day, 3) a few hours after the overshoots at 12:00 UTC on 7 August, and 4)
174 the aircraft measurement time at 06:00 UTC on 8 August 2017. There exist several tropopause definitions,

175 considering temperature lapse rate, potential vorticity, and static stability (WMO, 1957; Maddox and
176 Mullendore, 2018). In this study, the overshoots are defined as convective cloud tops that reach the
177 lowermost stratosphere above 380 K level. This simple definition is sufficient enough to study the impact of
178 convective hydration on the TTL as it quickly returns to its undisturbed state (Dauhut et al., 2018). A tracer
179 of tropospheric air is also calculated on line during the Meso-NH run. At the simulation initiation, the
180 tropospheric and stratospheric air masses are divided by a boundary at 380 K level, and the tracer values are
181 set to 1 and 0 below and above, respectively. In other words, pure concentration of tropospheric
182 (stratospheric) air has tracer value equal to 100 (0) %.

183

184 **3. Convective hydration in the TTL**

185 *3.1. Moistened layers in the TTL*

186 FISH and FLASH instruments on board flight #7 measure moisture and ice content in the TTL to the south of
187 Kathmandu along the track of $\sim 85.2^\circ\text{E}$, $25\text{--}26.5^\circ\text{N}$ (blue line in Fig. 1) from 06:20 to 06:48 UTC on 8
188 August 2017. ML and IL were observed. ML is evident at altitudes of 18–19 km by the water vapour content
189 of 4.8–5.7 ppmv (solid line in Fig. 2a), and IL is apparent at altitudes of 17–18 km with the ice content of up
190 to 1.9 eq. ppmv (solid line in Fig. 2b) and water vapour of 3.3–5.0 ppmv (solid line in Fig. 2a). The
191 temperature minimum, which defines the cold point tropopause (CPT, red line in Fig. 2c), equals -83.5°C at
192 17.8 km in between ML and IL (black line in Fig. 2c). In ML, the potential temperature ranges between 394
193 and 428 K, while in IL it ranges between 372 and 393 K (blue line in Fig. 2c). Figure 2d shows that RH_{ice}
194 increases beyond 70 % in ML and IL, and that IL is partly super-saturated with RH_{ice} up to 118 %. In both
195 ML and IL, strong easterly wind prevails (black line in Fig. 2e) with wind speed exceeding 20 m s^{-1} (blue
196 line in Fig. 2e), while easterlies stronger than 30 m s^{-1} are seen at 17 and 18.5 km altitudes.

197 Figure 2 also evidences that Meso-NH succeeds in reproducing most of the measurements in the TTL.
198 It reproduces the enhanced amount of water vapour in both ML and IL. In ML, the simulated water vapour in
199 the range between 4.9–6.0 ppmv with an average value (black cross marks in Fig. 2a) of 5.5 ppmv
200 reproduces the measured 4.2–5.6 ppmv well. In IL, the appearance of ice (black cross marks in Fig. 2b) is
201 simulated, but with a maximum value of 0.65 eq. ppmv, a factor of 3 less compared to the measured
202 concentrations. The simulation captures well the CPT at 17.8 km altitude and -83.3°C (cross marks in Fig.

203 2c), RH_{ice} values of 70–100 % between 16.5–18.5-km altitudes (cross marks in Fig. 2d), and the strong
204 easterly wind (black and blue cross marks in Fig. 2e). Despite small vertical variations in water vapour and
205 temperature that are missing around the CPT, the simulation is good enough to being used to investigate the
206 source and the pathways of water in ML and IL.

207 A few hours before the Geophysica measurements and upstream, some clouds were observed in the
208 TTL by CALIOP around 20:00 UTC on 7 August 2017. Figure 3a shows a V-shaped region of strong
209 backscatter values of $0.001\text{--}0.008\text{ km}^{-1}\text{ sr}^{-1}$ from 15 to 18.5 km altitudes over India along the track of
210 $25.5\text{--}31.5^\circ\text{N}$ (yellow line in Fig. 1). The V-shaped strong backscatter region is successfully reproduced by
211 Meso-NH (Fig. 3b) at 15–18.5-km altitudes between 26.5 and 31°N but with backscatter values lower than
212 measured. The simulated V-shaped region is characterized by low ice content (≥ 0.1 eq. ppmv, Fig. 3c) while
213 an above-background amount of water vapour of 5–7 ppmv is layered at altitudes higher than 18 km, (Fig.
214 3d), where ML is located. The V-shaped strong backscatter region is possibly induced by waves propagating
215 at these high altitudes, e.g. gravity waves. Investigating the mechanism at its origin is however beyond the
216 scope of this article. It is worth noting that the above-background water vapour concentration and the ice
217 content are already upstream ($93\text{--}95^\circ\text{E}$) about 10 hours before flight #7 ($\sim 85.2^\circ\text{E}$) and that Meso-NH is able
218 to resolve clouds in the UTLS.

219

220 3.2. Target convective overshoots

221 In the region where ML and IL are located, the simulated hydration patch (water vapour ≥ 5.2 ppmv) is in
222 evidence at the 410 K level at 06:00 UTC on 8 August 2017 (Fig. 4a). It is positioned above high-level
223 clouds, as shown with BT values lower than -47°C in both the SEVIRI/MSG imagery and the Meso-NH
224 simulation in Fig. 5a and 5b (pointed by arrows), respectively. This hydration patch has been advected from
225 the east by the strong easterlies (about 25 m s^{-1} , see Fig. 2e). At 12:00 UTC on 7 August, it is located around
226 eastern India (Fig. 4c) and is associated with low BT values ($\leq -55^\circ\text{C}$) in both the MSG/SEVIRI imagery
227 (pointed by an arrow in Fig. 5c) and the Meso-NH simulation (Fig. 5d). This suggests that the hydration
228 patch is generated by the injection of water by convective overshoots. The convective overshoots start to be
229 seen from 14:00 UTC on 6 August over the Sichuan basin (Fig. 4e), and they develop in this region until
230 21:00 UTC. During the period between 14:00 and 21:00 UTC, the developing overshoots collectively inject a
231 large water vapour hourly budget of 896 t above the CPT (as the result of integrating the water vapour

232 content between two isentropic altitudes of 380 and 530 K). The signature of overshoots is evidenced over
233 the Sichuan basin at 21:00 UTC by the large amount of water vapour in excess of 18 ppmv at 410 K level
234 (Fig. 4d) and by BT values lower than -80°C (Fig. 5e and 5f). At 13:00 UTC before the overshoot
235 development, neither water vapour mixing ratio larger than 5 ppmv nor BT values lower than -60°C are
236 distinguishable over the Sichuan basin (box in Fig. 5g and 5h).

237 In summary, a good agreement is achieved between the measurements (airborne and spaceborne) and
238 the Meso-NH simulation. The analysis of the simulation shows that the water-enhanced layers in ML and IL
239 observed to the south of Kathmandu around 06:30 UTC on 8 August were generated by the injection of water
240 by the convective overshoots produced over the Sichuan basin during 14:00–21:00 UTC on 6 August.

241

242 **4. Pathway of the hydration patch and processes affecting it**

243 *4.1. Evolution of the hydration patch during its way to the south of Kathmandu*

244 The hydration patch is described along its way from the Sichuan basin to the south of Kathmandu. In the
245 following, vertical sections of water vapour, ice content and tropospheric tracer are shown across the
246 hydration patch in the west-east orientation every 2 to 6 h (Figs. 6, 7, and 8). The vertical cross-sections are
247 centred over the hydration patch, all with the same size.

248

249 *4.1.1. Injection of water into the TTL by convective overshoots*

250 The vertical cross-sections of water vapour and ice content evidence that the large amounts of water vapour
251 and ice are injected above 380 K level by the convective overshoots that occurred during 15:00–21:00 UTC
252 on 6 August. At 13:00 UTC (Fig. 6a), just before the overshoot development, a strong upward motion is seen
253 at 16–18-km altitudes, while the cloud top (black solid line) is located in IL (about 17.5 km), just below the
254 CPT. At 15:00 UTC (Fig. 6b), a large amount of water vapour (≥ 15 ppmv) is in evidence in ML above 410
255 K level while a large ice content in excess of 120 eq. ppmv is found in IL, between 380 and 410 K levels
256 (Fig. 7b). Figure 8a–b shows that during 15:00–17:00 UTC the concentration of the tropospheric tracer
257 increases in both ML and IL with values of 4 and 30 %, respectively.

258 At 17:00 UTC and even higher cloud top is apparent at ~ 19.5 km altitude (Fig. 6c), a large amount of
259 water vapour (≥ 18 ppmv) rises to ~ 20 km, around 103°E , and a large ice content (≥ 120 eq. ppmv) stays
260 below 18 km altitude (Fig. 7c). The large amount of water is directly injected by convective overshoots

261 mainly in the form of ice, as the ice-laden air within the convective overshoots mixes with the entrained
262 stratospheric air during the collapse of the overshooting top. The warm, sub-saturated stratospheric air causes
263 the ice to rapidly sublimate into water vapour at the top of the overshoot, moistening the layer. It is worth
264 noting the water injected by the convective overshoots at 15:00 UTC is still apparent in ML at 17:00 UTC
265 around 102°E with a water vapour mixing ratio above 9 ppmv (Fig. 6c). In a similar way, the convectively-
266 injected large moisture at 17:00 UTC around 103°E (Fig. 6c) is found in ML at 19:00 UTC around 102.5°E
267 with a water vapour mixing ratio larger than 15 ppmv (Fig. 6d). At 19:00 UTC (Fig. 6d), the strong
268 convective updraughts perturb the isentropic surfaces (red solid lines), descending the 410 K level largely
269 from about 18.5 to 17.5 km. At 21:00 UTC a higher cloud top is found above ML in a wide area
270 (102.3–103.3°E longitude). The injected water vapour (≥ 18 ppmv) is transported above 20.5 km (Fig. 6e)
271 while the concentration of 0.1–0.5 % of the tropospheric tracer is seen in the water vapour pocket. The large
272 ice content exceeding 120 eq. ppmv is distributed mostly in IL (Fig. 7e). During 15:00–21:00 UTC (Fig.
273 8b–e), a concentration of 2–20 % of the tropospheric tracer is consistently seen in ML, while higher
274 concentration of 40 % has been found in IL. During 17:00–21:00 UTC (Fig. 9c–e), the large turbulent
275 kinetic energy (TKE) of $0.2\text{--}0.9\text{ m}^2\text{ s}^{-2}$ is apparent in a limited area of cloud top ($\sim 103^\circ\text{E}$).

276 *4.1.2. Evolution of the hydration patch along its pathway*

277 From 23:00 UTC on 6 August to 06:00 UTC on 8 August 2017, the convective overshoots gradually
278 diminish in the region of longitude $\sim 98\text{--}85^\circ\text{E}$ and latitude $\sim 28\text{--}25^\circ\text{N}$ (see Fig. 4). At 23:00 and 00:00 UTC,
279 the anvil-shaped cloud above 16 km altitude presents a rather flat cloud top around 19 km (Fig. 7f and 7g).
280 The injected large amount of water vapour ≥ 18 ppmv is evident in ML, even at higher altitudes up to 20.5
281 km (Fig. 6f and 6g) whereas the large ice content ≥ 120 eq. ppmv is no longer apparent in IL (Fig. 7f and 7g).
282 Within the anvil cloud, still large TKE of $0.2\text{--}0.9\text{ m}^2\text{ s}^{-2}$ is seen (Fig. 9f, g). During 06:00–18:00 UTC on 7
283 August, the water vapour mixing ratio in ML gradually decreases from 15 to ~ 9 ppmv, meanwhile the air
284 mass in IL becomes dry with a water vapour mixing ratio below 4 ppmv (Fig. 6h–j). During the same period,
285 the increase of tropospheric tracer concentration and TKE are evident in both ML and IL. The air mass with
286 concentration higher than 40 % is apparent in IL while the air mass with a lower tropospheric concentration
287 around 0.02–0.3 is seen in IL (Fig. 8h–j).

288 The air mass with high tropospheric tracer concentration of 2–40 % consistently exists in ML and IL
289 from 00:00 to 06:00 UTC on 8 August 2017 (Fig. 8k–l), while the TKE of $0.2\text{--}0.9\text{ m}^2\text{ s}^{-2}$ exists in wide area

290 between the altitudes of 16 and 18 km (Fig. 9k–l). During this period, the hydration patch is further narrowed
291 and widened in ML (Fig. 6k–l), and the air mass becomes drier in IL (≤ 3 ppmv). Note that the even low
292 numerical diffusion of the PPM scheme also contributes to the dispersion of the hydration patch. At 00:00
293 UTC (Fig. 7k), new convection tops are apparent in altitudes of 16–17 km, and an increase of ice content
294 above 3 eq. ppmv is seen in IL. Then a decrease of ice content down to 0.1–1 eq. ppmv distributes in IL at
295 06:00 UTC where large ice content around 1–1.9 eq. ppmv was measured (see Fig. 2b).

296

297 *4.2. Processes affecting the hydration patch*

298 The processes that affect the moist and ice layers are further described. To this objective, average quantities
299 are calculated in ML and IL. The hourly evolution of water vapour, ice content, temperature, and RH_{ice}
300 shows the lifetime of the injected water in ML and IL along the pathway of the hydration patch (Fig. 10). The
301 profiles of tropospheric tracer, temperature, RH_{ice} , water vapour, ice content and wind speed give a vertical
302 view in the column across the tropical tropopause layer (Fig. 11). A scatter plot using tropospheric tracer and
303 water vapour highlights the mixing processes occurring in the hydration patch (Fig. 12).

304

305 *4.2.1. Mixing of the overshoots with the stratospheric air*

306 The hourly evolution of the average water vapour and the ice content along the pathway of the hydrated layer
307 demonstrates the hydration in the TTL by the convective overshoots (Fig. 10). During the development of the
308 convective overshoots between 14:00 and 21:00 UTC on 6 August 2017, the average water vapour mixing
309 ratio increases to 5.7 ppmv in IL (yellow solid line, Fig. 10a), while a large mixing ratio of 6.5 ppmv is seen
310 in ML (blue solid line in Fig. 10a). The ice content reaches more than 200 eq. ppmv in both layers and more
311 than 300 eq. ppmv in IL (Fig. 10b). Until 17:00 UTC, the temperature increases in both layers (solid lines in
312 Fig. 10c), indicating the mixing with the warmer stratospheric air. Because of this entrained stratospheric air,
313 RH_{ice} decreases largely below 60 % in ML (blue line with symbols in Fig. 10c), and down to 90 % in IL
314 (yellow line with symbols). Due to the mixing with entrained warmer stratospheric air, the enriched water
315 vapour layer then remains at this higher isentropic level after the overshoot collapses. The conditions and
316 timescale of the detailed process trapping the enriched water vapour in the TTL was demonstrated by Dauhut
317 et al. (2018). Thanks to a fine temporal resolution of 1 min, they revealed that this process occurs on short
318 time scales within 20 min. The active mixing of the convective overshoots with the stratospheric air between

319 14:00 and 21:00 UTC is also evidenced by the evolution of vertical profiles of tropospheric tracer (Fig. 11a).
320 The tropospheric tracer concentration increases from 0 to 5 % in ML (yellow to green lines in Fig. 11a),
321 while the stratospheric air concentration (1 minus tracer) increases of 5 % in IL. The temperature increases in
322 both ML and IL (yellow to green lines in Fig. 11b) where the relative humidity decreases (yellow to green
323 lines in Fig. 11c).

324 The scatter plot of the tropospheric tracer and water vapour mixing ratio (Fig. 12) evidences the large
325 mixing of tropospheric and stratospheric air masses in the TTL (14–22 km altitudes). A large evolution of the
326 tropospheric tracer–water vapour diagram is found from 13:00 to 21:00 UTC on 6 August (Fig. 12a and
327 12b). At 13:00 UTC before the development of the convective overshoots, the air mass with potential
328 temperature (θ) of 410–420 K (yellow dots), corresponding to ML, is relatively dry with a water vapour
329 mixing ratio of 5–7.2 ppmv (Fig. 12a) and very small compounds of tropospheric air (tracer ≤ 0.1 %). The
330 air mass with θ of 380–390 K (black dots), corresponding to IL, has a low water vapour mixing ratio of
331 3–7.5 ppmv. At 21:00 UTC (Fig. 12b), the air mass with θ between 410 and 420 K becomes very humid
332 (5.5–13.6 ppmv of water vapour) and the concentration of tropospheric tracer increases to 0.2–8 %.
333 Moreover the air mass with very-high θ of 450–460 K (purple dots) is moistened largely as shown by a water
334 vapour mixing ratio above 15 ppmv. So does the air mass with θ between 390 and 410 K, which is both
335 moistened and enriched by the tropospheric tracer with a concentration of 5–60 % (red to orange dots, Fig.
336 12b). The convective overshoots also impact the air mass below the CPT by widening the range of the water
337 vapour mixing ratio with θ between 370 and 380 K (grey dots in Fig. 12a and b) from 3.2–13.9 ppmv at
338 13:00 UTC (Fig. 12a) to 0–18.8 ppmv at 21:00 UTC (Fig 12b).

339 From 17:00 UTC on 6 August to 02:00 UTC on 7 August, Fig. 9c shows that the temperature
340 decreases gradually (solid lines), while the relative humidity increases (lines with symbols). In ML and IL, a
341 great part of ice contents, especially snow and graupel fall quickly (dashed line in Fig. 10b), and the rest
342 sublimates. Meanwhile ice sediment out, still there is a low concentration of cloud ice in both ML and IL,
343 and the water vapour concentration slightly decreases (blue solid line in Fig. 10a). The continued presence of
344 cloud ice in ML suggests that the ice may have formed in-situ in response to wave-driven temperature
345 oscillations that locally drive the RH to ice saturation. The ice microphysics might play a pivotal role in
346 controlling the eventual moisture content since ice nucleation and the subsequent ice-growth process to
347 deplete slowly the ML. In ML, the relative humidity increases (in range of 65–80 %) mainly due to the

348 temperature decrease (in range of -78 and -82°C) (solid lines, Fig. 10c). During this period, the easterly
349 wind is nearly constant with the relatively-weak speed of $\sim 15\text{ m s}^{-1}$ in ML and $\sim 16.5\text{ m s}^{-1}$ in IL (yellow to
350 green lines, Fig. 11f). After 7 August, in ML, the relative humidity less than 80 % indicates strong sub-
351 saturation where a very small amount (0.1–0.3 eq. ppmv) of cloud ice still resides. This is probably induced
352 by the domain-averaged analysis.

353

354 4.2.2. Processes occurring in the hydration patch during the advection

355 After the development of the convective overshoots, the hydration patch travels westward across India and
356 north Bangladesh from 21:00 UTC on 6 August to 06:00 UTC on 8 August (Fig. 4). During its travel, the air
357 mass in ML and IL has less and less amount of water vapour and ice content (Fig. 10a–b).

358 Between 21:00 UTC on 6 August and 12:00 UTC on 7 August, the concentration of tropospheric tracer
359 increases at high altitudes with θ between 410 and 420 K up to 18 % (yellow dots, Fig. 12b–c). At the same
360 time, the water vapour decreases by a factor of two, in the range of 5–9.6 ppmv. This can be also seen in the
361 vertical profiles for which the concentration of tropospheric tracer increases at 12:00 UTC on 7 August in
362 both ML and IL (green to blue lines, Fig. 11a) and the water vapour decreases (green to blue lines, Fig. 11d).
363 The two layers become colder by $\sim 3^{\circ}\text{C}$ (green to blue lines in Fig. 11b), and dehydrated compared to the
364 initial state of 13:00 UTC on 6 August (yellow line in Fig. 11d, e). It includes much reduced amount of ice
365 content (green to blue solid lines in Fig. 11e), but still there exist ice content ≥ 1 eq. ppmv and cloud ice \geq
366 0.5 eq. ppmv at 12:00 UTC on 7 August (blue dashed line, Fig. 11e). In IL (Fig. 10c), RH_{ice} oscillates mostly
367 driven by temperature variation. Over time, the air mass in ML and IL gets colder and less humid by the
368 lowered cloud top below 17 km altitude. In both ML and IL, the easterly winds weaken below 15 m s^{-1} .
369 Moreover, the turbulent kinetic energy (TKE) increases from 0.1–0.3 $\text{m}^2\text{ s}^{-2}$ at 21:00 UTC to 0.2–0.9 $\text{m}^2\text{ s}^{-2}$
370 at 12:00 UTC in ML and IL (Fig. 9e, i). These results suggest that the water vapour concentration in ML and
371 IL decreases due to the turbulent diffusion in both the vertical and the horizontal direction consistent with the
372 increase of tropospheric tracer. Also, the vapour-scavenging effect by ice nucleation and particle growth
373 within IL contributes to reduce the water vapour deriving the dehydration. The rapid decrease of ice content
374 in IL due to both sublimation and sedimentation (Fig. 7f–i) results in the lowering of the cloud top from 17
375 to below 16 km at $97\text{--}101^{\circ}\text{E}$ at 06:00 UTC (Fig. 7h), and finally to 15 km around 95.5°E at 12:00 UTC (Fig.
376 7i).

377 Further increased tropospheric tracer concentration is distinguished from 12:00 UTC on 7 August to
378 06:00 UTC on 8 August 2017 in ML and IL (blue to red lines, Fig. 11a). Moreover the tropospheric tracer
379 concentration reaches to about 30 and 70 % in ML and IL, respectively while the water vapour decreases
380 (Fig. 11a and 11d). During this time, the cloud top height of convective cloud descends below 14 km (Fig.
381 6i–l), where RH_{ice} dramatically decreases (Figs. 2d, 11c). The entrained cold tropospheric air (and/or colder
382 background air) and the hydrostatic adjustment decrease the temperature in ML and IL (Fig. 11b). It is worth
383 noting the shape of the temperature profile that becomes straight upward in the altitudes of 17–18.5 km
384 during the overshoot activity (green line, Fig. 11b). Also it is worth noting the decrease of ice content less
385 than 0.3 eq. ppmv (blue to red line, Fig. 11e), and the large-decrease of relative humidity in altitudes below
386 17.5 km.

387 The increased tropospheric tracer concentration in ML and IL is as well seen by the tracer–vapour
388 diagram of Fig. 12c–d. The concentration of tropospheric tracer increases at high altitudes with θ between
389 410 and 420 K (yellow dots) up to 20 % at 06:00 UTC on 8 August 2017, meanwhile the tropospheric air
390 concentration increases up to 50 % at the altitudes with θ between 390 and 400 K (red dots in Fig. 12d).
391 During the period (12:00 UTC on 7 August to 06:00 UTC on 8 August), the water vapour decreases in all
392 altitudes with θ above 380 K (Fig. 12c–d). It decreases from 9.6 to below 6.2 ppmv in ML (θ between
393 410–430 K, yellow and green dots) while dropping below 5 ppmv in IL (θ between 380–400 K, red and
394 black dots). The reduced ice content in ML and IL might be induced by sublimation due to the mixing with
395 the dry tropospheric air ($RH_{ice} \sim 50\text{--}70\%$) of below 16 km level (red line in Fig. 11c and cross marks in Fig.
396 2d). The air mixing of tropospheric and stratospheric air masses might be induced by the vertical wind shear
397 with the maxima wind speeds in excess of 30 m s^{-1} at ~ 17 and 18.5 km altitudes (see Fig. 2e, average value
398 in range of 18 and 25 m s^{-1} of red line in Fig. 11f). With the strengthened easterlies, the air mass in IL is well
399 mixed rather than conserved in this layer. Also, this wind shear layer with a large gradient of wind speed
400 ($25\text{--}35\text{ m s}^{-1}$) locates below and above the CPT (Fig. 2c, 2e), thus it results in the strait upward temperature
401 profile with the constant value about -80°C at 06:00 UTC on 8 August as seen in Fig. 10b (red line). The air
402 mass in ML and IL has large TKE values of $0.5\text{ m}^2\text{ s}^{-2}$ (Fig. 9l).

403

404 5. Conclusions

405 The source and pathway of the hydration patch in the TTL (Tropical Tropopause Layer) that was measured

406 during flight #7 of the StratoClim 2017 field campaign during the Asian summer monsoon, and its
407 connection to overshooting convection are investigated. During the Geophysica flight #7 around 06:30 UTC
408 on 8 August 2017, two remarkable layers were observed to the south of Kathmandu above and below the
409 CPT located at 17.8 km, a moist layer (ML) with large water vapour content of 4.2–5.6 ppmv in altitudes of
410 18–19 km in the lower stratosphere, and an ice layer (IL) with large ice content up to 1.9 eq. ppmv at
411 altitudes of 17–18 km in the upper troposphere. The Meso-NH numerical simulation run with a 2.5 km
412 horizontal grid spacing succeeds in reproducing ML and IL. Through analysis using airborne and spaceborne
413 measurements and the numerical simulation, we show that the measured hydration patch in ML found in the
414 south of Kathmandu ($\sim 85^\circ\text{E}$) was produced by the convective overshoots that occurred over the Sichuan
415 basin ($\sim 103^\circ\text{E}$) between 14:00 and 21:00 UTC on 6 August 2017. The key hydration processes are
416 summarized schematically in Fig. 13.

417 The convective overshoots develop up to 19.5 km altitude in the Sichuan basin, and transport large
418 amount of water vapour of 6.5 ppmv to ML and ice content in excess of 300 eq. ppmv to IL. Between 15:00
419 and 21:00 UTC, the overshooting clouds collectively hydrate the lower stratosphere resulting in the total
420 amount of water vapour of 6088 t. It is also worth noting the large concentration of water vapour of over 18
421 ppmv up to 20 km level which is above the convective cloud top of 19.5 km (a yellow ellipsoid in Fig. 13a).
422 This feature is similarly seen during the development of the Hector the Convective in the Tiwi Islands
423 (Dauhut et al., 2018), however, the magnitude is ~ 10 ppmv higher in the present event. The concentration of
424 the tropospheric tracer reaches to 8 and $\sim 60\%$ in ML and IL, respectively, indicating the strong mixing of
425 the convective updraughts with the stratospheric air (black arrows in Fig. 13a). The strong convective
426 updraughts perturb the isentropic surfaces (red line in Fig. 13a), descending the 410 K level from 18.5 to
427 17.5 km. During these convective events, the mixing of the tropospheric and stratospheric air masses
428 increases the temperature in ML and IL. Moreover, the moderate -not intense- easterly wind ($\sim 15\text{ m s}^{-1}$)
429 prevails constantly in these levels, and it does not interrupt the convection developing vigorously in altitude
430 (19.5 km ASL) and reaching the lower stratosphere.

431 The injected water by the convective overshoots generates the hydration patch, i.e. large water vapour
432 in ML (ellipse in Fig. 13b). During its westward travel, its altitude is kept constant by the moderate easterlies
433 of about 15 m s^{-1} in ML and IL. The tropospheric tracer concentration is continuously increased in these
434 layers, where the above-background amount of water vapour is still remained and where the ice content

435 gradually sediments out and forms again along the pathway. It is highlighted that the large transported
436 amount of water vapour (≥ 18 ppmv) still remains at high altitudes of up to 20.5 km even when the anvil
437 cloud top descends to 18.5 km. Later on, the cloud top is still seen around 16–17 km level, keeping the large
438 RH_{ice} (about 95 %) in these altitudes. A part of the water vapour has been lost due to ice formation and
439 sedimentation and the turbulent diffusion in both vertical and the horizontal direction (black arrows in Fig.
440 13b). The ice microphysics (e.g. nucleation, growth, and sedimentation of ice particles) might play a pivotal
441 role in controlling the eventual moisture content since ice nucleation and the subsequent growth process
442 would slowly deplete the water vapour. This falling of ice and a reduced updraught are evident by the
443 lowered cloud top height partly from 17 to ~ 15 km (Fig. 13c).

444 Then the hydration patch continues to travel to the south of Kathmandu, with even higher tropospheric
445 tracer concentration of ~ 30 and 70 % in ML and IL, respectively (darkened blue shades in Fig. 13c). During
446 the same period, the top of convective clouds further descends below 14 km, thus the layer below IL, i.e.
447 15–17 km, becomes dry with RH_{ice} below 70 %. Due to mixing with the dry tropospheric air, the remaining
448 water vapour in ML gradually diffused in horizontal and vertical direction (ellipse). It is also true that the ice
449 content in IL is locally influenced by new convection with cloud top in altitudes 16–17 km about 6 h before
450 flight #7. The continuous air mixing might be induced by the vertical wind shear in altitudes 15–19 km
451 where the wind speed varies from ~ 18 to 25 m s^{-1} (red bold arrows in Fig. 13c). The vertical mixing due to
452 wind shear modifies the temperature profile to the straight-upward in 17–18 km rather than bending. Also,
453 vertical motions caused by gravity waves breaking might play an important role in the transport of
454 tropospheric air into the TTL. In addition, after the strong updraughts of overshooting convection, the
455 remaining horizontal divergence in the lower stratosphere might let the tropospheric air continues to ascend.

456 Many of previous Lagrangian studies (Tzella and Legras, 2011; Tissier and Legras, 2016)
457 demonstrated the link between the moistened TTL and remote overshoots using large-scale numerical
458 simulations. Thanks to the combination of aircraft measurement and a 3-day convection-permitting
459 simulation, this study shed light on the processes along the pathway of a hydration patch from overshooting
460 clouds for 1.5 days, showing the 3-D evolution of water vapour and ice content.

461 This study focuses on the hydration patch that was measured during the last descending of flight #7
462 and the corresponding convective overshoots over the Sichuan basin. Here, the average water vapour amount
463 in the lower stratosphere is 6.5 ppmv during the convective event while a water vapour of 6 ppmv is found

464 above West Africa during the monsoon season by Khaykin et al. (2009). By comparison, convection
465 developing during the Asian monsoon over the Sichuan basin had a similar impact on the stratospheric water
466 budget as above West Africa. From the hourly budget of 869 t, we can also confirm that the local impact of
467 overshoots developed during the Asian summer monsoon is stronger than the one over tropical Africa
468 (300–500 t according to Liu et al., 2010) and is weaker than Hector the Convecton over the Tiwi Islands
469 (2776 t according to Dauhut et al., 2015). Because of a large variety in the lifetime and horizontal scale of
470 overshoots, an accumulation of more event-scale analyses is important. In addition, note that the amount of
471 injected moisture is sensitive to the grid spacing of simulation (up to a factor of 2 with horizontal grid
472 spacing varying from 1600 to 100 m; Dauhut et al., 2015) and the convection duration of target system. The
473 simple set up of tropospheric tracer of this study, i.e. tropospheric air below the 380 K isentropic altitude,
474 allows the mixture of tropospheric and stratospheric air parcels in the TTL by vigorous convective
475 overshoots to be understood. To estimate the detailed origin i.e. defining the lower, middle, and upper
476 troposphere, of air parcel, further analyses using passive tracers (e.g. Mullendore et al., 2005; Hassim and
477 Lane, 2010; Homeyer, 2015; Dauhut et al., 2016) will be required. Also, additional numerical simulation
478 with a 2-moment microphysical scheme that considers mass and number concentration of hydrometeors and
479 aerosol together with options in the turbulent scheme (e.g., 1D against 3D formulation, Machado and
480 Chaboureau, 2015) will be worthwhile to study the impact on the results. To understand how much water
481 vapour and ice are generally injected into the TTL through convective overshoots during the Asian summer
482 monsoon is currently investigated in a follow-up study. Further, it would be interesting to investigate the
483 transport of chemical constituents, e.g. methane, nitrogen oxides, and carbon monoxide, via convective
484 overshoots during this season.

485

486 **Data availability**

487 After the StratoClim embargo period, the aircraft data will be available at the DLR database [https://halo-](https://halo-db.pa.op.dlr.de/mission/101)
488 [db.pa.op.dlr.de/mission/101](https://halo-db.pa.op.dlr.de/mission/101). Meso-NH output data are available from JPC upon request.

489

490 **Author contribution**

491 KOL, TD and JPC designed the numerical simulation, and JPC performed the simulation. KOL, TD and JPC
492 designed the manuscript and analyses. SK provided the FLASH instrument data, and MK and CR provided

493 the FISH instrument data. KOL prepared the manuscript with contributions from all co-authors.

494

495 **Competing interests**

496 The authors declare that they have no conflict of interest.

497

498 **Acknowledgement**

499 This study is funded by the StratoClim project by the European Union Seventh Framework Programme
500 under grant agreement no 603557 and the IDEX TEASAO project. Computer resources were allocated by
501 GENCI through project 90569.

502

503 **References**

504 Afchine, A., Rolf, C., Costa, A., Spelten, N., Riese, M., Buchholz, B., Ebert, V., Heller, R., Kaufmann, S.,
505 Minikin, A., Voigt, C., Zöger, M., Smith, J., Lawson, P., Lykov, A., Khaykin, S., and Krämer, M.: Ice
506 particle sampling from aircraft – influence of the probing position on the ice water content, *Atmos.*
507 *Meas. Tech.*, 11, 4015-4031, <https://doi.org/10.5194/amt-11-4015-2018>, 2018.

508 Bougeault, P. and Lacarrère, P.: Parameterization of orography-induced turbulence in a meso-beta-scale
509 model. *Mon. Weather Rev.* 117(8): 1872–1890, <https://doi.org/10.1175%2F1520-0493%281989%29117%3C1872%3APOOITI%3E2.0.CO%3B2>, 1989.

511 Chaboureau, J.-P., Cammas, J.-P., Duron, J., Mascart, P. J., Sitnikov, N. M., and Voessing, H. J.: A numerical
512 study of tropical cross-tropopause transport by convective overshoots, *Atmos. Chem. Phys.*, 7, 1731–
513 1740, <https://doi.org/10.5194/acp-7-1731-2007>, 2007.

514 Chaboureau, J.-P., and Coauthors: A midlatitude precipitating cloud database validated with satellite
515 observations. *J. Appl. Meteor. Climatol.*, 47, 1337–1353, <https://doi.org/10.1175/2007JAMC1731.1>,
516 2008.

517 Chaboureau, J.-P., and Coauthors: Long-range transport of Saharan dust and its radiative impact on
518 precipitation forecast: A case study during the Convective and Orographically-induced Precipitation
519 Study (COPS). *Quart. J. Roy. Meteor. Soc.*, 137, 236–251, <https://doi.org/10.1002/qj.719>, 2011.

520 Colella, P. and Woodward, P. R.: The piecewise parabolic method (PPM) for gas dynamical simulations. *J.*

521 Comput. Phys. 54: 174–201, [https://doi.org/10.1016/0021-9991\(84\)90143-8](https://doi.org/10.1016/0021-9991(84)90143-8), 1984.

522 Cuxart, J., Bougeault, P., and Redelsperger, J. L.: A turbulence scheme allowing for mesoscale and large-
523 eddy simulations. *Q. J. R. Meteorol. Soc.* 126(562): 1–30, <https://doi.org/10.1002/qj.49712656202>,
524 2000.

525 Dauhut, T., Chaboureau, J. P., Escobar, J., and Mascart, P.: Large-eddy simulations of hector the convective
526 making the stratosphere wetter. *Atmos. Sci. Let.* 16, 135–140, <https://doi.org/10.1002/asl2.534>. 2015.

527 Dauhut, T., Chaboureau, J. P., Escobar, J., and Mascart, P.: Giga-LES of hector the convective and its two
528 tallest updrafts up to the stratosphere. *J. Atmos. Sci.*, 73, 5041–5060, <https://doi.org/10.1175/JAS-D-16-0083.1>, 2016.

529

530 Dauhut, T., Chaboureau, J. P., Haynes, P. H., and Lane, T. P.: The mechanisms leading to a stratospheric
531 hydration by overshooting convection. *J. Atmos. Sci.*, 75, 4383–4398, <https://doi.org/10.1175/JAS-D-18-0176.1>, 2018
532

533 Dessler, A. E. and Sherwood, S. C.: Effect of convection on the summertime extratropical lower stratosphere,
534 *J. Geophys. Res.*, 109, D23301, <https://doi.org/10.1029/2004JD005209>, 2004.

535 Fueglistaler, S., Dessler, A. E., Dunkerton, T. J., Folkins, I., Fu, Q., and Mote, P. W.: Tropical tropopause
536 layer, *Rev. Geophys.*, 47, RG1004, <https://doi.org/10.1029/2008RG000267>, 2009.

537 Funatsu, B. M., Rysman, J. F., Claud, C., and Chaboureau, J. P.: Deep convective clouds distribution over the
538 Mediterranean region from AMSU-B/MHS observations, *Atmos. Res.*, 207, 122–135,
539 <https://doi.org/10.1016/j.atmosres.2018.03.003>, 2018.

540 Gal-Chen, T. and Somerville, R. C. J.: On the use of a coordinate transformation for the solution of the
541 Navier-Stokes equations. *J. Comput. Phys.* 17: 209–228, [https://doi.org/10.1016/0021-9991\(75\)90037-6](https://doi.org/10.1016/0021-9991(75)90037-6), 1975.
542

543 Homeyer, C. R., Pan, L. L., Dorsi, S. W., Avallone, L. M., Weinheimer, A. J., O'Brien, A. S., DiGangi, J. P.,
544 Zondlo, M. A., Ryerson, T. B., Diskin, G. S., and Campos, T. L.: Convective transport of water vapor
545 into the lower stratosphere observed during double-tropopause events. *J. Geophys. Res. Atmos.*, 119,
546 10941–10958, <https://doi.org/10.1002/2014JD021485>, 2014.

547 Homeyer, C. R.: Numerical simulations of extratropical tropopause penetrating convection, *J. Geophys. Res.*
548 *Atmos.*, 120, 7174–7188. <https://doi.org/10.1002/2015JD023356>, 2015.

549 Homeyer, C. R., McAuliffe, J. D., and Bedka, K. M.: On the development of above-anvil cirrus plumes in

550 Extratropical convection. *J. Atmos. Sci.*, 74, 1617–1633, <https://doi.org/10.1175/JAS-D-16-0269.1>,
551 2017

552 Hassim, M. E. E. and Lane, T. P.: A model study on the influence of overshooting convection on TTL water
553 vapour, *Atmos. Chem. Phys.*, 10, 9833–9849, <https://doi.org/10.5149/acp-10-9833-2010>, 2010.

554 Highwood, E. J., and Hoskins, B. J.: The tropical tropopause, *Q. J. R. Meteorol. Soc.*, 124, 1579–1604,
555 <https://doi.org/10.1002/qj.49712454911>, 1998.

556 Hoskins, B. J. and Rodwell, M. J.: A model of the Asian summer monsoon, I, The global scale, *J. Atmos. Sci.*,
557 52, 1329–1340, <https://doi.org/10.1175/1520-0469%281995%29052%3C1329%3AAMOTAS%3E2.0.CO%3B2>, 1995.

559 Jensen, E., Ackerman, A. S. and Smith, J. A.: Can overshooting convection dehydrate the tropical tropopause
560 layer? *J. Geophys. Res.*, 112, D11209, <https://doi.org/10.1029/2006JD007943>, 2007.

561 Kato T.: Structure of the band-shaped precipitation system inducing the heavy rainfall observed over
562 northern Kyushu, Japan on 29 June 1999. *J. Meteor. Soc. Japan.* 84,129–153,
563 <https://doi.org/10.2151/jmsj.84.129>, 2006.

564 Khaykin, S. M., Pommereau, J.-P., Riviere, E. D., Held, G., Ploeger, F., Gysels, M., Amarouches, N., Vernier,
565 J.-P., Wienhold, F. G., and Ionov, D.: Evidence of horizontal and vertical transport of water in the
566 southern hemisphere tropical tropopause layer (TTL) from high-resolution balloon observation,
567 *Atmos. Chem. Phys.*, 16, 12273–12286, <https://doi.org/10.5194/acp-16-12273-2016>, 2016.

568 Khaykin, S., Pommereau, J.-P., Korshunov, L., Yushkov, V., Nielsen, J., Larsen, N., Christense, T., Garnier,
569 A., Lukyanov, A., and Williams, E.: Hydration of the lower stratosphere by ice crystal geysers over
570 land convective systems, 9, 2275–2287, <https://doi.org/10.5194/acp-9-2275-2009>, 2009.

571 Khaykin, S. M., Engel, I., Vömel, H., Formanyuk, I. M., Kivi, R., Korshunov, L. I., Krämer, M., Lykov, A.
572 D., Meier, S., Naebert, T., Pitts, M. C., Santee, M. L., Spelten, N., Wienhold, F. G., Yushkov, V. A., and
573 Peter, T.: Arctic stratospheric dehydration – Part 1: Unprecedented observation of vertical
574 redistribution of water, *Atmos. Chem. Phys.*, 13, 11503–11517, [https://doi.org/10.5194/acp-13-11503-](https://doi.org/10.5194/acp-13-11503-2013)
575 2013, 2013.

576 Lac, C., Chaboureaud, J. P., Masson, V., Pinty, J. P., Tulet, P., Escobar, J., Leriche, M., Barthe, C., Aouizerats,
577 B., Augros, C., Aumond, P., Auguste, F., Bechtold, P., Berthet, S., Bieilli, S., Bosseur, F., Caumont, O.,
578 Cohard, J. M., Colin, J., Couvreur, F., Cuxart, J., Delautier, J., Dauhut, T., Ducrocq, V., Filippi, J.B.,

579 Gazen, D., Geoffroy, O., Gheusi, F., Honnert, R., Lafore, J. P., Lebeaupin, Brossier C., Libois, Q.,
580 Lunet, T., Mari, C., Maric, T., Mascart, P., Mogé, M., Molinié, G., Nuissier, O., Pantillon, F., Peyrillé,
581 P., Pergaud, J., Perraud, E., Pianezze, J., Redelsperger, J. L., Ricard, D., Richard, E., Riette, S., Rodier,
582 Q., Schoetter, R., Seyfried, L., Stein, J., Suhre, K., Taufour, M., Thouron, O., Turner, S., Verrelle, S.,
583 Vié, B., Visentin, F., Vionnet, V., and Wautelet, P.: Overview of the Meso-NH model version 5.4 and
584 its applications. *Geosci. Model Dev.*, 11, 1929–1969, <https://doi.org/10.5194/gmd-11-1929-2018>, 2018.

585 Lee, K. O., Flamant, C., Ducrocq, V., Duffourg, F., Fourrié, N., and Davolio, S. : Convective initiation and
586 maintenance processes of two back-building mesoscale convective systems leading two heavy
587 precipitation events in South Italy during HyMeX IOP 13. *Q. J. R. Meteorol. Soc.*, 142, 2623–2635,
588 <https://doi.org/10.1002/qj.2851>, 2016.

589 Liu, C., and Zipser, E. J.: Global distribution of convection penetrating the tropical tropopause, *J. Geophys.*
590 *Res.*, 110, D23104, <https://doi.org/10.1029/2005JD006063>, 2005.

591 Liu, X. M., Rivière, E. D., Marécal, V., Durry, G., Hamdouni, A., Arteta, J., and Khaykin, S.: Stratospheric
592 water vapour budget and convection overshooting the tropopause: modelling study from SCOUT-
593 AMMA. *Atmos. Chem. Phys.*, 10, 8267–8286, www.atmos-chem-phys.net/10/8267/2010, 2010.

594 Machado, L. A., and Chaboureaud, J. P.: Effect of Turbulence Parameterization on Assessment of Cloud
595 Organization. *Mon. Wea. Rev.*, 143, 3246–3262, <https://doi.org/10.1175/MWR-D-14-00393.1>, 2015.

596 Maddox, E. M. and Mullendore, G. L.: Determination of best tropopause definition for convective
597 transportation studies. *J. Atmos. Sci.*, 75, 3433–3446, <https://doi.org/10.1175/JAS-D-18-0032.1>, 2018.

598 Mason, R. and Anderson, C.: The development and decay of the 100-MB. Summertime anticyclone over
599 southern Asia. *Mon. Wea. Rev.*, 1, 3–12, <https://doi.org/10.1175/1520-0493%281963%29091%3C0003%3ATDADOT%3E2.3.CO%3B2>, 1963.

600

601 Meyer, J., Rolf, C., Schiller, C., Rohs, S., Spelten, N., Afchine, A., Zöger, M., Sitnikov, N., Thornberry, T. D.,
602 Rollins, A. W., Bozóki, Z., Tátrai, D., Ebert, V., Kühnreich, B., Mackrodt, P., Möhler, O., Saathoff, H.,
603 Rosenlof, K. H., and Krämer, M.: Two decades of water vapor measurements with the FISH
604 fluorescence hygrometer: a review, *Atmos. Chem. Phys.*, 15, 8521–8538, <https://doi.org/10.5194/acp-15-8521-2015>, 2015.

605

606 Mullendore, G. L., Durran, D. R., and Holton, J. R.: Cross-Tropopause tracer transport in midlatitude
607 convection, *J. Geophys. Res.*, 110, D06113, <https://doi.org/10.1029/2004JD005059>, 2005.

608 Müller, R.: The performance of classical versus modern finite-volume advection schemes for atmospheric
609 modelling in a one-dimensional test-bed, *Mon. Wea. Rev.*, 120, 1407–1415,
610 [https://doi.org/10.1175/1520-0493\(1992\)120%3C1407:TPOCVM%3E2.0.CO;2](https://doi.org/10.1175/1520-0493(1992)120%3C1407:TPOCVM%3E2.0.CO;2), 1992.

611 Park, M., Randel, W. J., Kinnison, E. J., Garcia, R. R., and Choi, W.: Seasonal variation of methane, water
612 vapor and nitrogen oxides near the tropopause: Satellite observations and model simulation, *J.*
613 *Geophys. Res.*, 109, D03302, <https://doi.org/10.1029/2003JD003706>, 2004.

614 Pinty, J. P. and Jabouille, P.: A mixed-phased cloud parametrization for use in a mesoscale non-hydrostatic
615 model: Simulations of a squall line and of orographic precipitation. In: *Proc. Of the Conference on*
616 *Cloud Physics*. Amer. Meteorol. Soc, Boston: Everett, WA, USA, 17–21 Aug. 1998. Pp. 217–220,
617 1998.

618 Randel, W. J. and Park, M.: Deep convective influence on the Asian summer monsoon anticyclone and
619 associated tracer variability observed with Atmospheric Infrared Sounder (AIRS), *J. Geophys. Res.*,
620 111, D12314, <https://doi.org/10.1029/2005JD006490>, 2006.

621 Randel, W. J., Wu, F., Gettelman, A., Russell, J. M., Zawodny, J. M., and Oltmans, S. J.: Seasonal variation
622 of water vapour in the lower stratosphere observed in Halogen Occultation Experiment data, *J.*
623 *Geophys. Res.*, 106(D13), 14313–14325, <https://doi.org/10.1029/2001JD900048>, 2001.

624 Rysman, J. F., Claud, C., Chaboureau, J. P., Delanoë, J., and Funatsu, B. M.: Severe convection in the
625 Mediterranean from microwave observations and a convection-permitting model, *Quart. J. Roy.*
626 *Meteor. Soc.*, 142, 43-55, <https://doi.org/10.1002/qj.2611>, 2016.

627 Rolf, C., Vogel, B., Hoor, P., Afchine, A., Günther, G., Krämer, M., Müller, R., Müller, S., Spelten, N., and
628 Riese, M.: Water vapor increase in the lower stratosphere of the northern hemisphere due to the Asian
629 monsoon anticyclone observed during the TACTS/ESMVal campaigns, *Atmos. Chem. Phys.*, 18,
630 2973–2983, <http://doi.org/10.5194/acp-18-2973-2018>, 2018.

631 Saunders, R., Hocking, J., Rundle, D., Rayer, P., Matricardi, M., Geer, A., Lupu, C., Brunel, P., and Vidot, J.:
632 RTTOV-11—Science and validation report. NWP SAF Tech. Rep., 62 pp., 2013.

633 Shu, C. W. and Osher, S.: Efficient implementation of essentially non-oscillatory shock-capturing schemes.
634 *Journal of Computational Physics* 77(2): 439–471, [https://doi.org/10.1016/0021-9991\(88\)90177-5](https://doi.org/10.1016/0021-9991(88)90177-5),
635 1988.

636 Sitnikov, N. M., Yushkov, V. A., Afchine, A. A., Korshunov, L. I., Astakhov, V. I., Elanovskii, A. E., Kraemer,

637 M., Mangold, A., Schiller, C., and Ravegnani, F.: The FLASH instrument for water vapor
638 measurements on board the high-altitude airplane. *Instrum. Exp. Tech.*, 50, 113–121,
639 <https://doi.org/10.1134/S0020441207010174>, 2007.

640 Smith, J. B., Wilmouth, D. M., Bedka, K. M., Bowman, K. P., Homeyer, C. R., Dykema, J. A., Sargent, M.
641 R., Clapp, C. E., Leroy, S. S., Sayres, D. S., Dean-Day, J. M., Bui, T. P., and Anderson, J. G.: A case
642 study of convectively sourced water vapor observed in the overworld stratosphere over the United
643 States. *J. Geophys. Res.*, 122, 9529–9554, <https://doi.org/10.1002/2017JD026831>, 2017.

644 Tissier, A.-S. and Legras, B.: Convective sources of trajectories traversing the tropical tropopause layer.
645 *Atmos. Chem. Phys.*, 16, 3383–3398, <https://doi.org/10.5194/acp-16-3383-2016>, 2016.

646 Tzella, A. and Legras, B.: A Lagrangian particle dispersion model FLEXPART version 6.2. *Atmos. Chem.*
647 *Phys.*, 5, 2461–2474, <https://doi.org/10.5194/acp-5-2461-2005>, 2005.

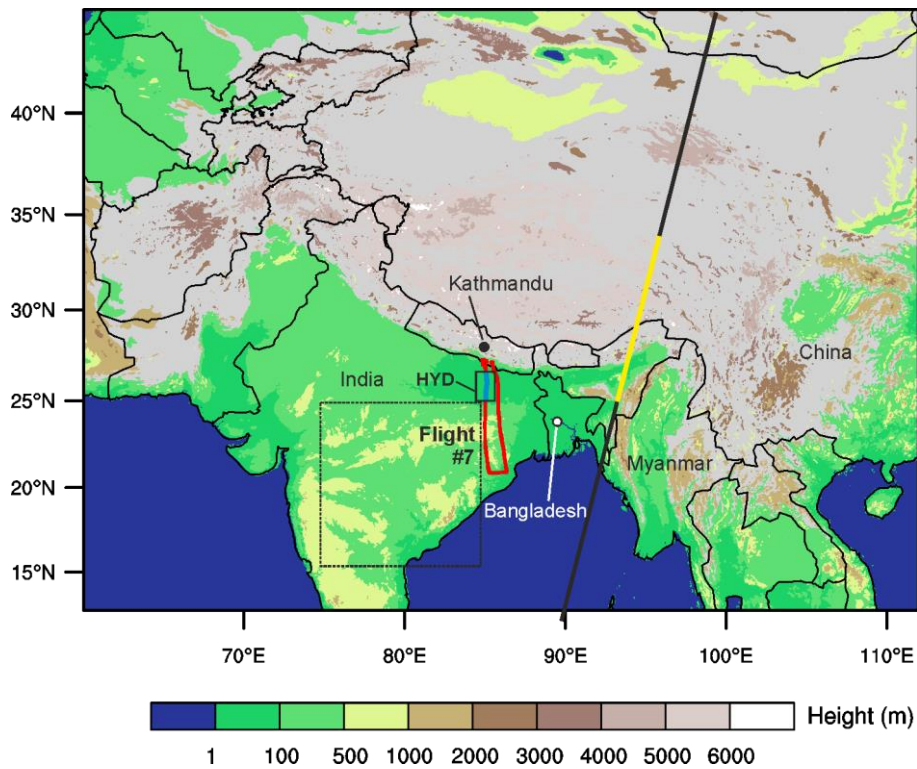
648 Winker, D. M., Vaughan, M. A., Omar, A., Hu, Y., Powell, K. A., Liu, Z., Hunt, W. H., and Young, S. A.:
649 Overview of the CALIPSO mission and CALIOP data processing algorithms. *J. Atmos. Oceanic*
650 *Technol.*, 26, 2310–2323, <https://doi.org/10.1175/2009JTECHA1281.1>, 2009.

651 WMO: Definition of the tropopause, *WMO Bull.*, 6, 136, 1957.

652 Wright, J. S., Fu, R., Fueglistaler, S., Liu, Y. S., and Zhang, Y.: The influence of summertime convection over
653 Southeast Asia on water vapor in the tropical stratosphere. *J. Geophys. Res.*, 116, D12302,
654 <https://doi.org/10.1029/2010JD015416>, 2011.

655 Zöger, M., Afchine, A., Eicke, N., Gerhards, M.-T., Klein, E., McKenna, D., Mörschel, U., Schmidt, U., Tan,
656 V., Tuitjer, F., Woyke, T., and Schiller, C.: Fast in situ stratospheric hygrometers: A new family of
657 balloon-borne and airborne Lyman-photofragment fluorescence hygrometers, *J. Geophys. Res.*, 104,
658 1807–1816, <https://doi.org/10.1029/1998JD100025>, 1999.

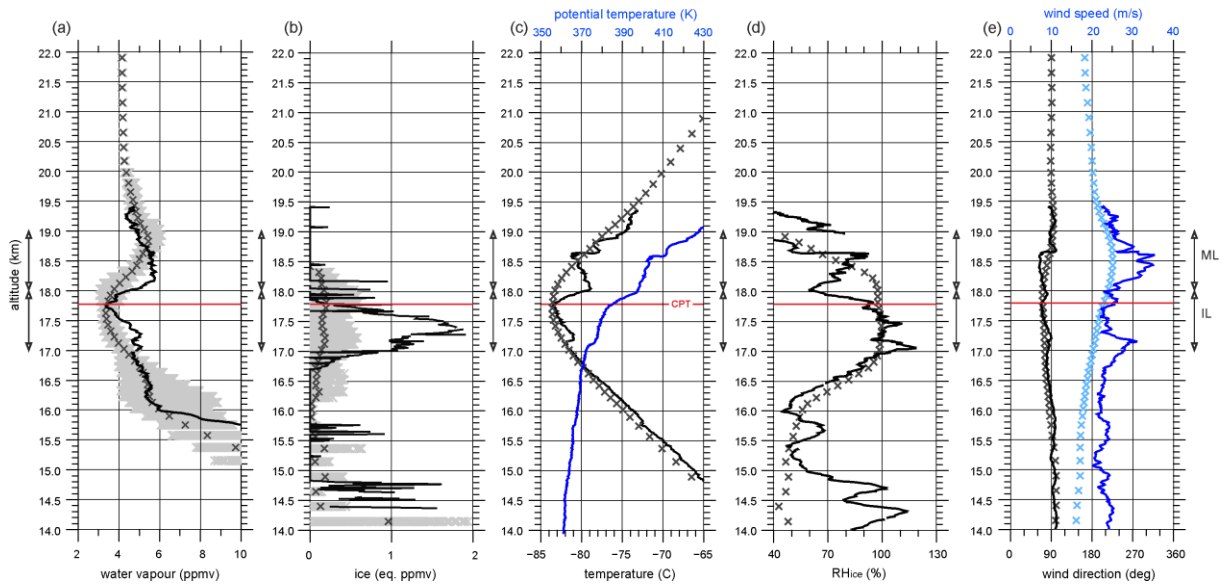
659



660

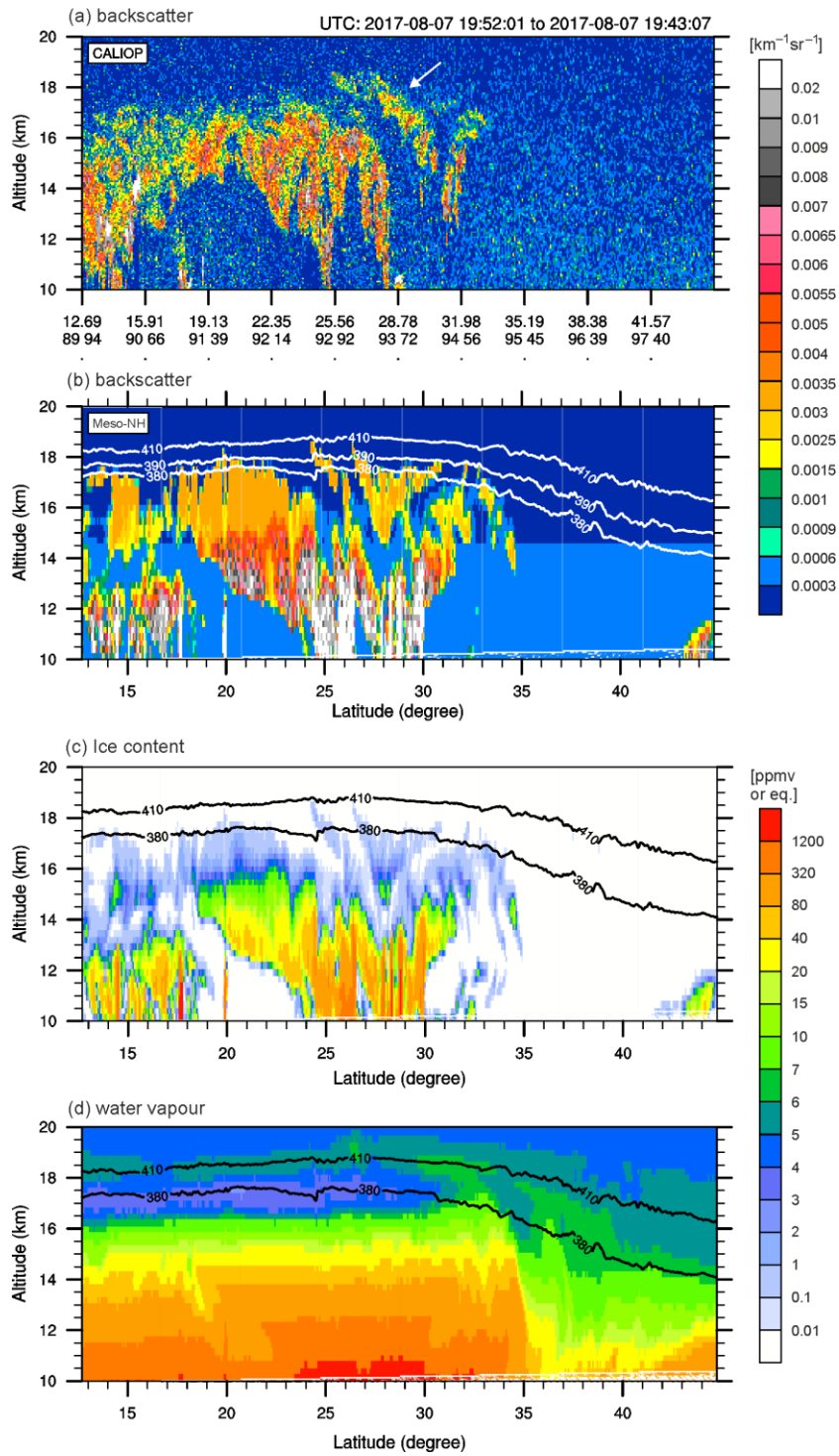
661 **Figure 1.** Topography and domain considered in the Meso-NH numerical simulation with a resolution of 2.5 km. The trajectory of
 662 the Geophysica flight #7 to the south of Kathmandu is shown by the red solid line, while the pathway of moist patch (25–26.5°N) is
 663 depicted by the blue line. A black box ‘HYD’ is a model domain considered in comparison with aircraft measurement. Another box
 664 with dashed line is a model domain used to calculate the background water vapour at 06:00 UTC on 8 August 2017. The track of
 665 CALIOP around 20:00 UTC on 7 August 2017 is shown by the black solid line while its track between 25 and 33°N is highlighted in
 666 yellow.

667



668

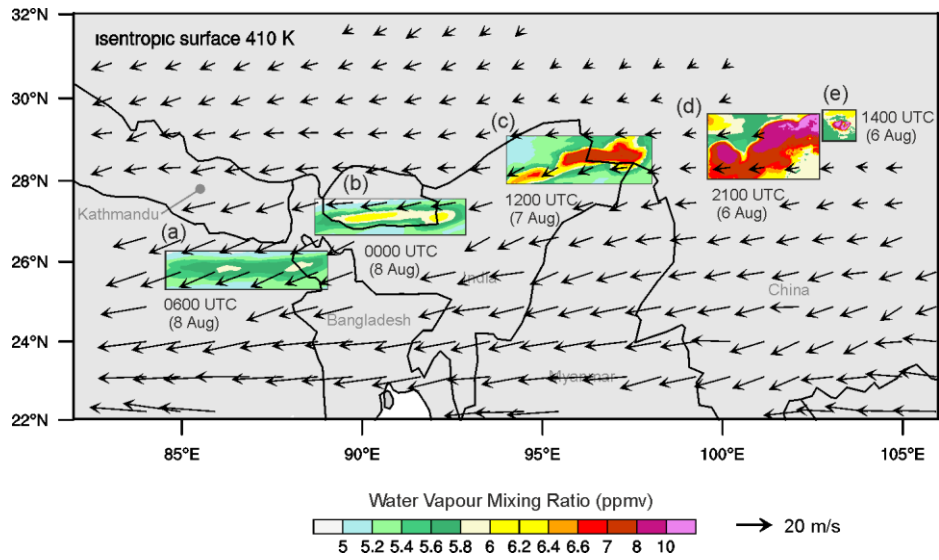
669 **Figure 2.** Vertical profiles of (a) water vapour (ppmv), (b) ice (eq. ppmv), (c) temperature ($^{\circ}\text{C}$) and potential temperature (K), (d)
 670 relative humidity respect to ice (RH_{ice} , %), and (e) wind direction (degree) and speed (m s^{-1}). In (a)–(e), the measured values along
 671 the blue-coloured track between $25\text{--}26.5^{\circ}\text{N}$ (shown in Fig. 1) from 06:20 to 06:48 UTC on 8 August 2017 are shown as solid line,
 672 while the domain averaged values in the region ‘HYD’ ($25\text{--}26.5^{\circ}\text{N}$, $85\text{--}85.5^{\circ}\text{E}$, shown in Fig. 1) from the Meso-NH simulation at
 673 06:00 UTC on the same day are shown as cross marks. In (a)–(e), the level of cold point tropopause (CPT) is indicated by a red line.
 674 In (a)–(b), all the values from Meso-NH within the ‘HYD’ is displayed by grey cross marks. The layers of ML and IL are marked by
 675 arrows.



676

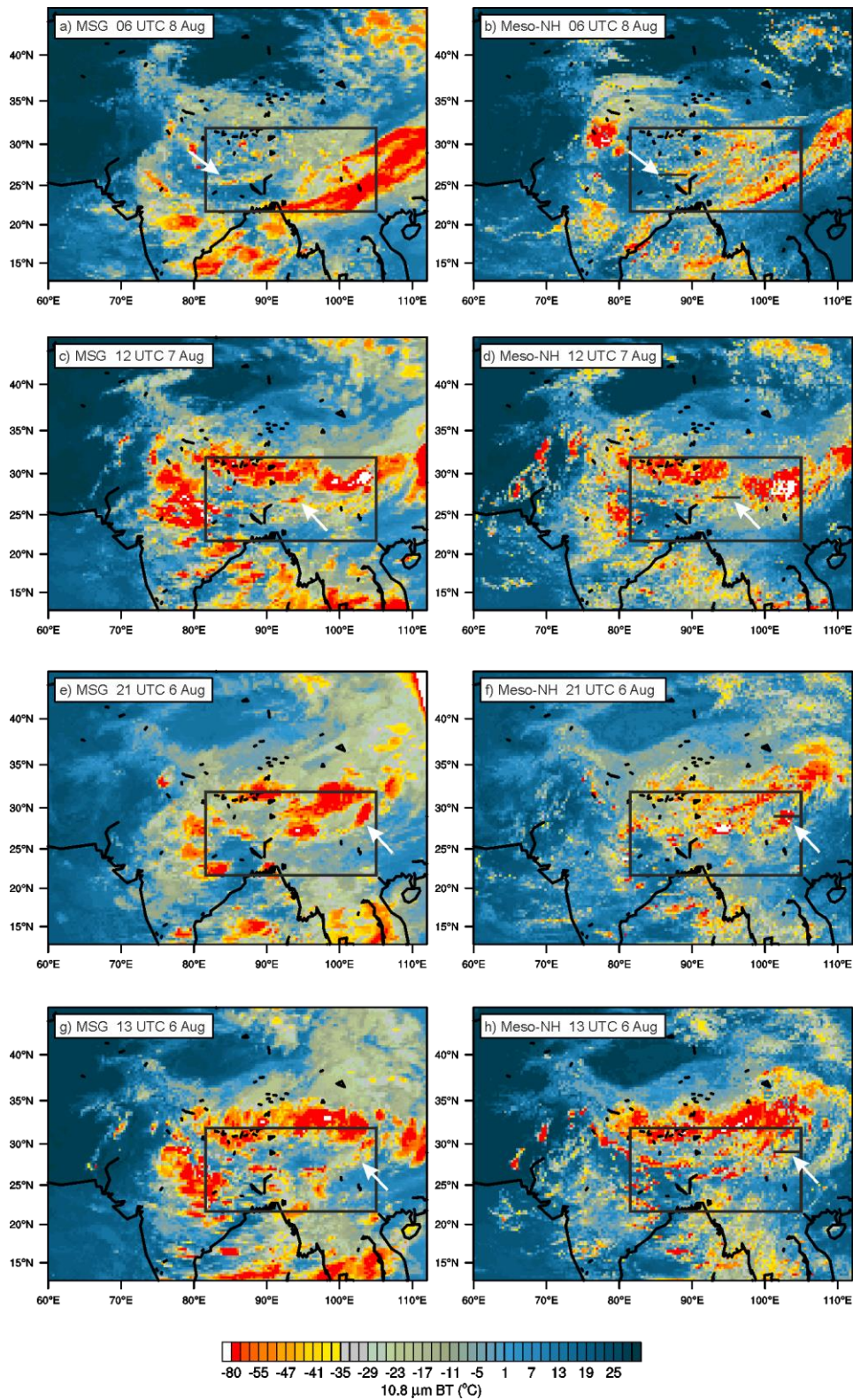
677 **Figure 3.** Backscatters at 532 nm (a) measured by CALIOP around 20:00 UTC and (b) retrieved by the Meso-NH simulation, and (c)
 678 ice content (eq. ppmv) and (d) water vapour (ppmv) produced by the Meso-NH simulation along the CALIOP track (marked by solid
 679 line in Fig. 1) at 20:00 UTC on 7 August 2017.

680



681

682 **Figure 4.** Target moist patch. Horizontal distribution of water vapour mixing ratio at 410 K isentropic altitude at (a) 06:00 UTC, and
 683 (b) 00:00 UTC on 8 August, (c) 12:00 UTC on 7 August, (d) 21:00 UTC and (e) 14:00 UTC on 6 August 2017. The horizontal wind
 684 at the altitude of 19 km (about 410 K isentrope) at 06:00 UTC on 8 August is displayed by vectors.



685

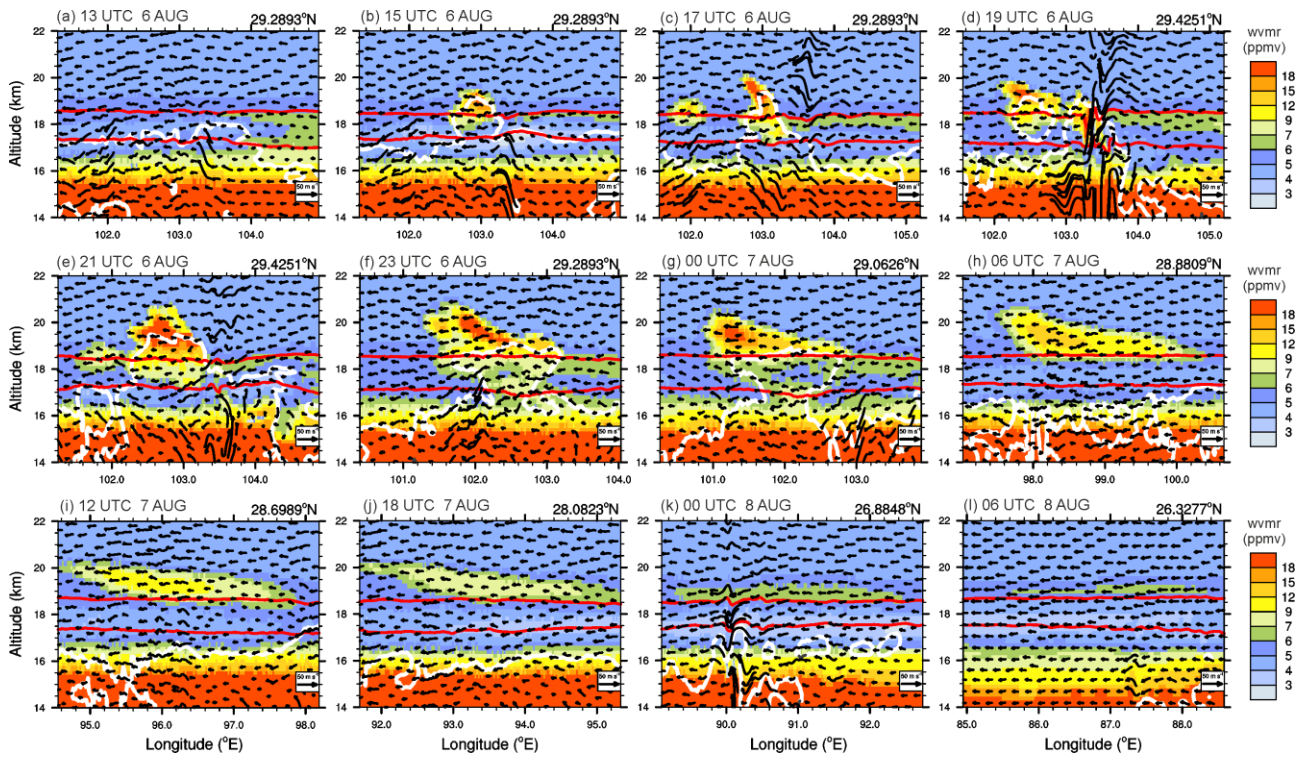
686

687

688

689

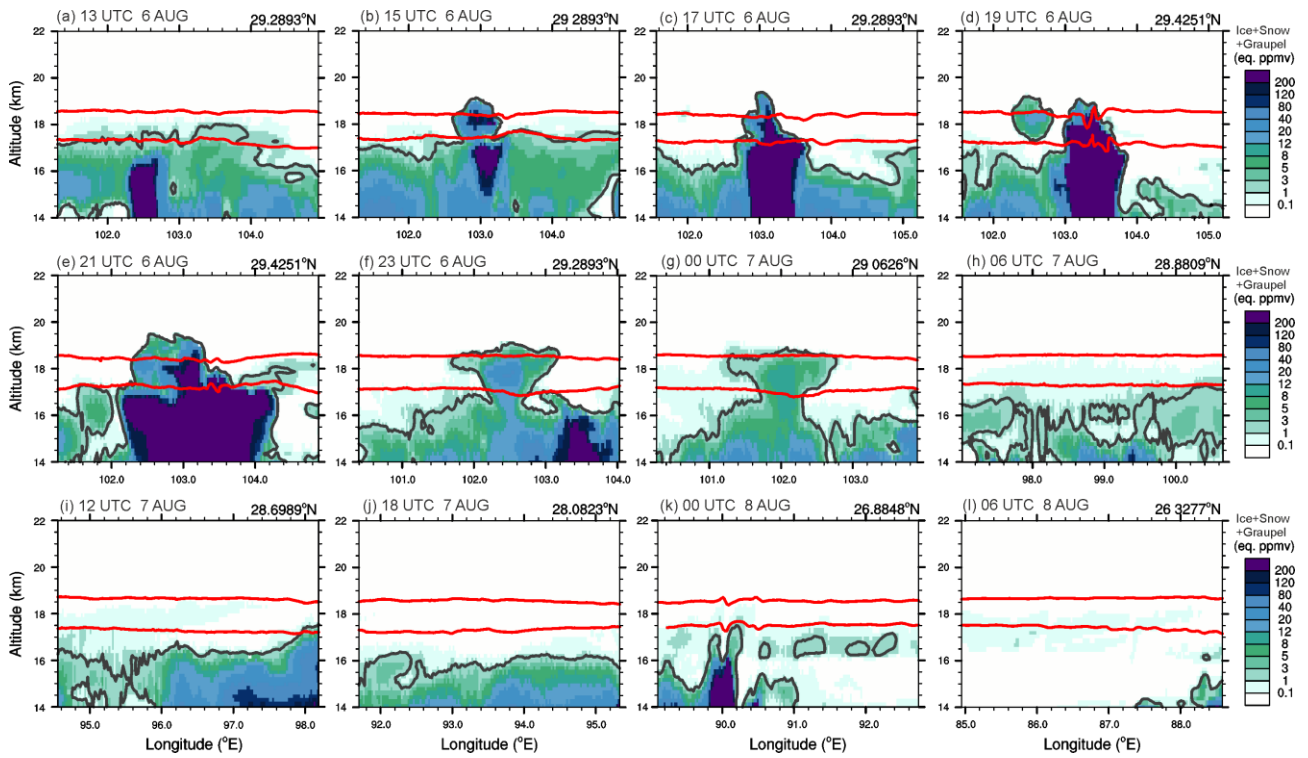
Figure 5. BT 10.8 μm obtained from SEVIRI/MSG (left) and Meso-NH (right) at (a)–(b) 06:00 UTC on 8 August, (c)–(d) 12:00 UTC on 7 August, (e)–(f) 21:00 UTC, and (f)–(h) 13:00 UTC on 6 August 2017. The domain used in Figure 4 is marked by a box in each panel, while the location of vertical cross-sections used in Figures 6–9 is marked by a black solid line in the right panels. The location of hydration patch is depicted by the white arrows.



690
691

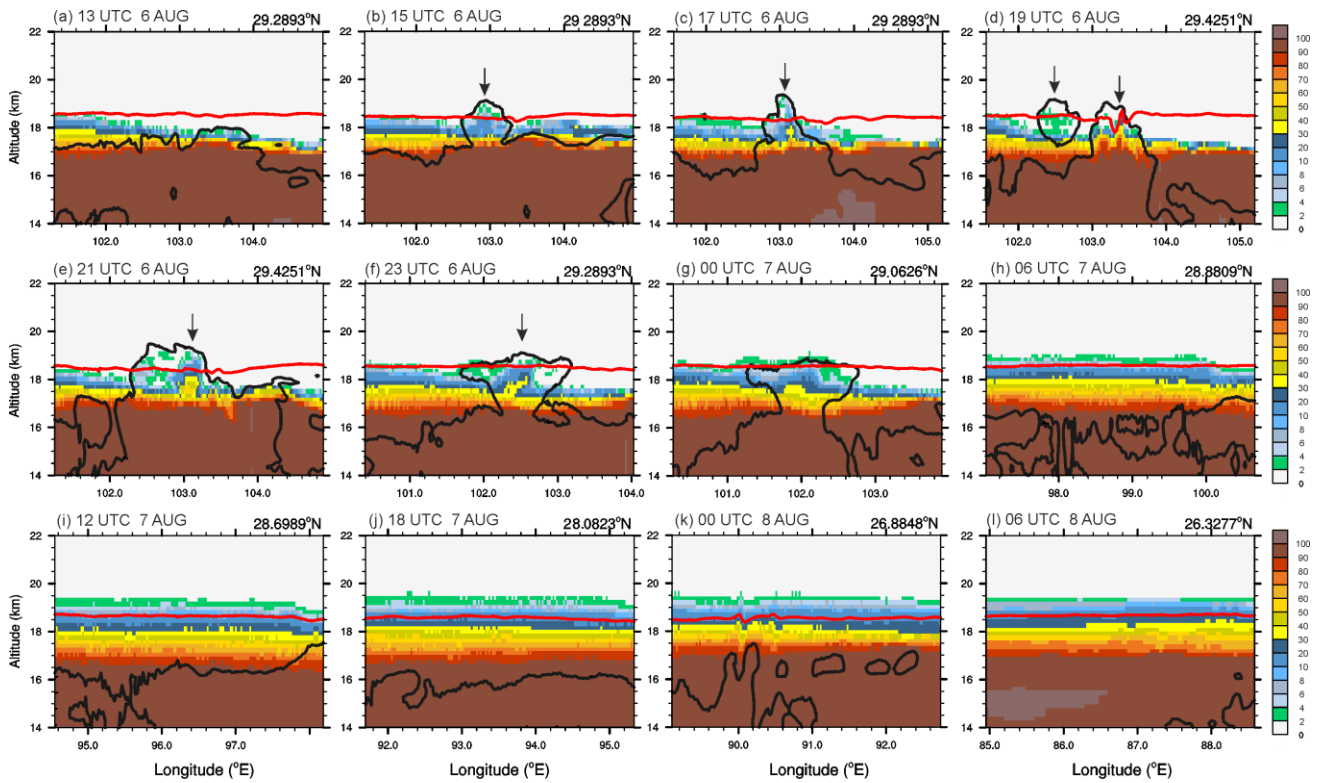
692 **Figure 6.** Vertical cross-sections of water vapour mixing ratio (shading) and wind (vectors) (a) 13:00 UTC, (b) 15:00 UTC, (c) 17:00
 693 UTC, (d) 19:00 UTC, (e) 21:00 UTC, (f) 23:00 UTC on 6 August 2017, (g) 00:00 UTC, (h) 06:00 UTC, (i) 12:00 UTC, (j) 18:00
 694 UTC on 7 August 2017, and (k) 00:00 UTC and (l) 06:00 UTC on 8 August 2017. The isentropic altitudes of 380 and 410 K are
 695 depicted by the red lines. The latitude (°N) of west-east oriented cross-section line is indicated at the upper right of each panel. The
 696 cloud boundary (mixing ratio of ice content of 10 mg kg^{-1}) is contoured by the white solid line.

697



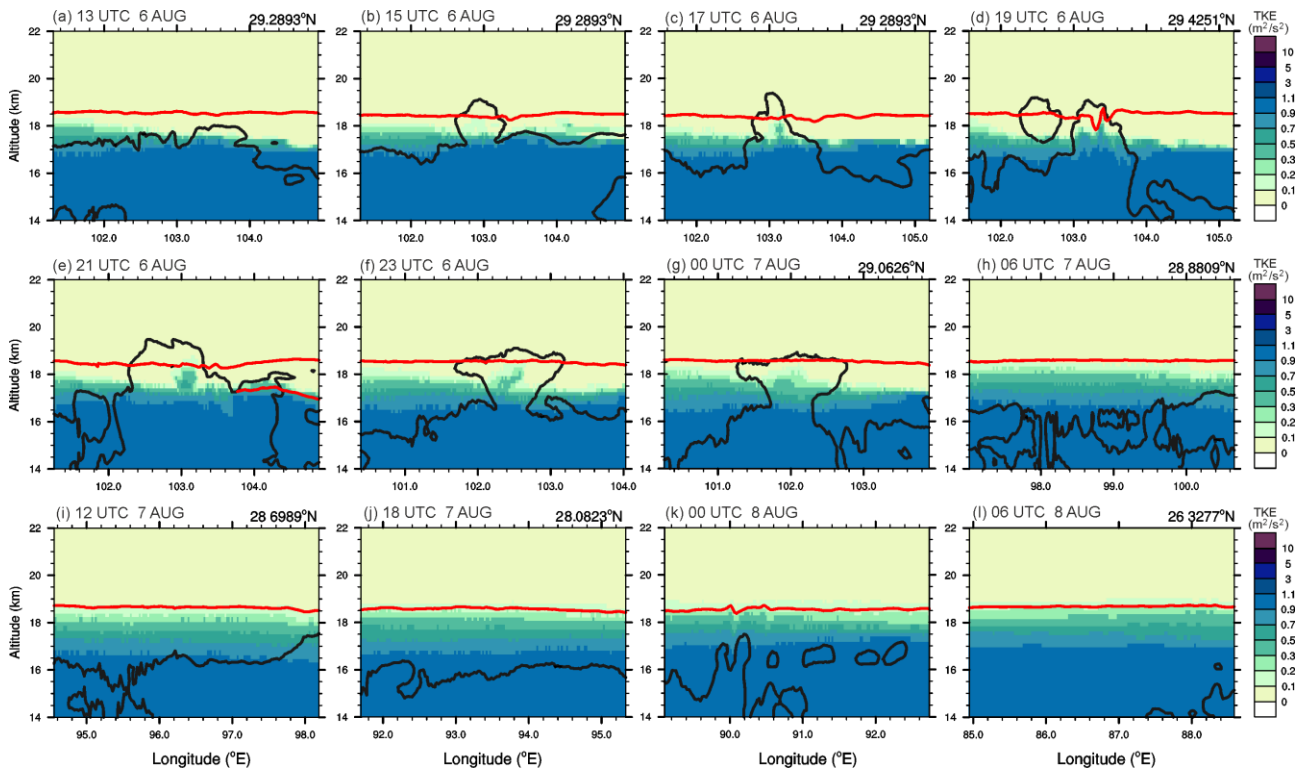
698
699
700
701
702

Figure 7. Same as Fig. 6 but for the ice content. The isentropic altitudes of 380 and 410 K are depicted by the red lines.



703
704
705
706

Figure 8. Same as Fig. 6 but for the tracer (%). The isentropic altitude of 410 K is depicted by the red line. The changes of the tropospheric tracer by convective overshoots is marked by downward arrows.

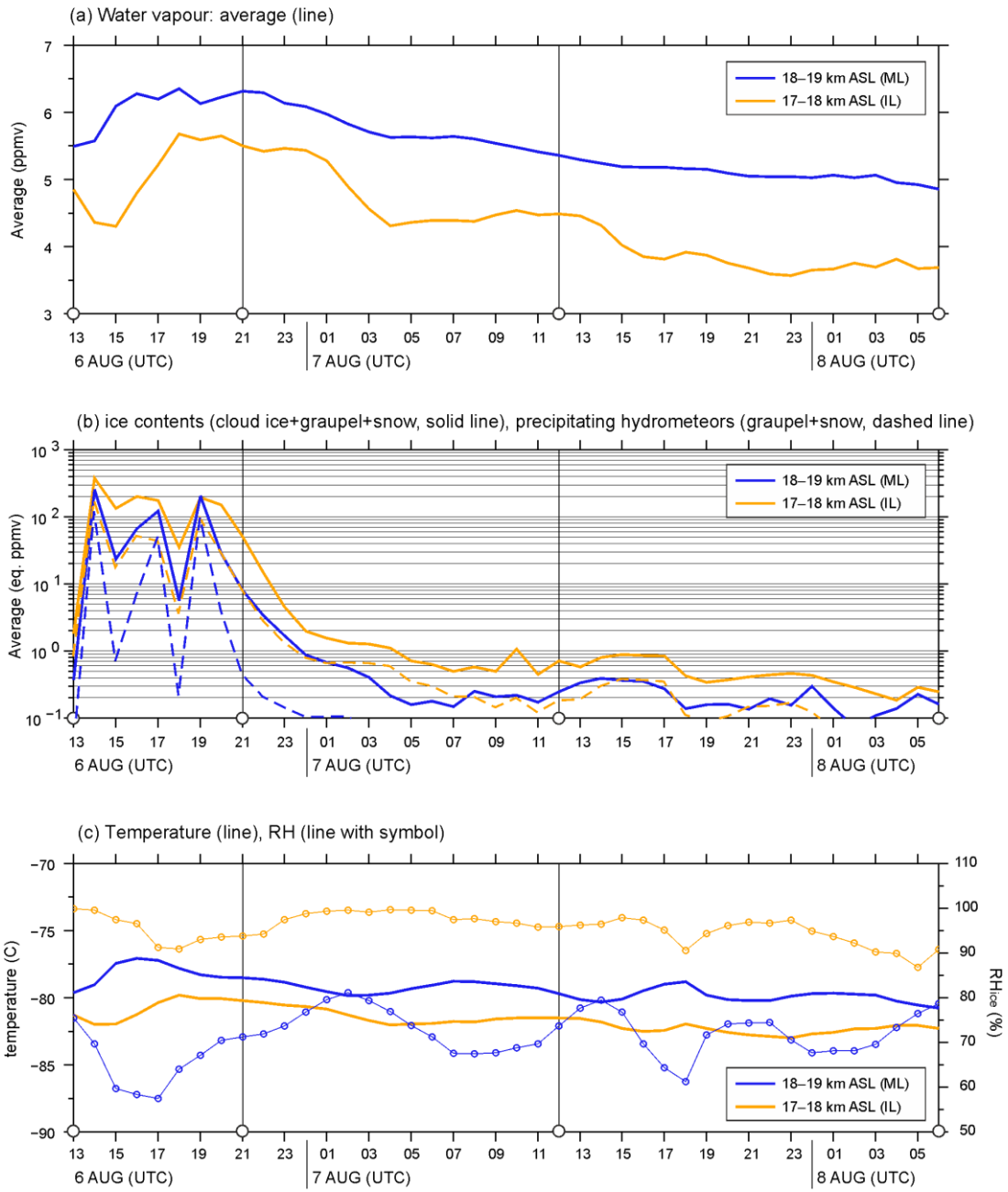


707

708

709 **Figure 9.** Same as Fig. 6 but for the TKE. The isentropic altitude of 410 K is depicted by the red line.

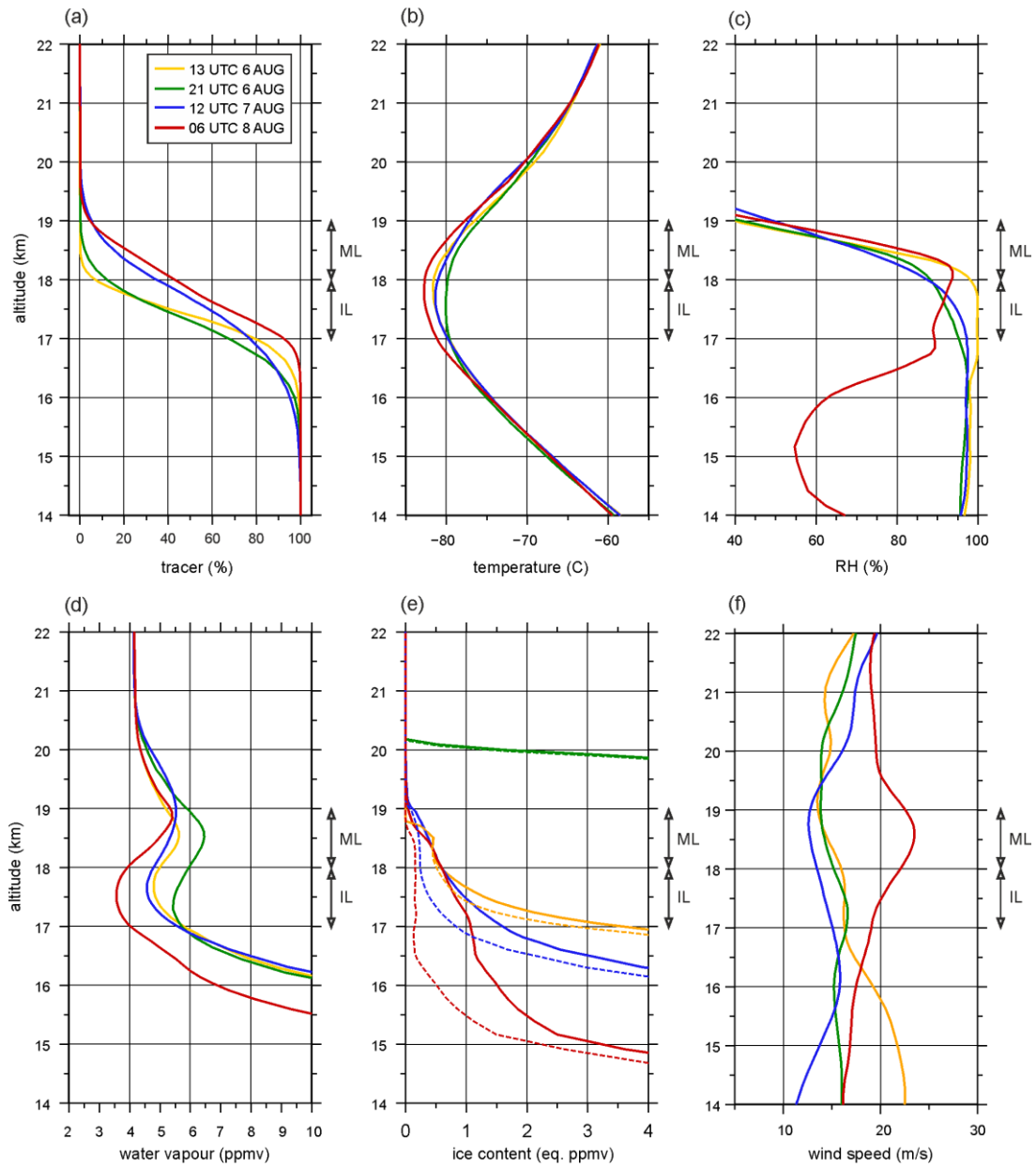
710



711

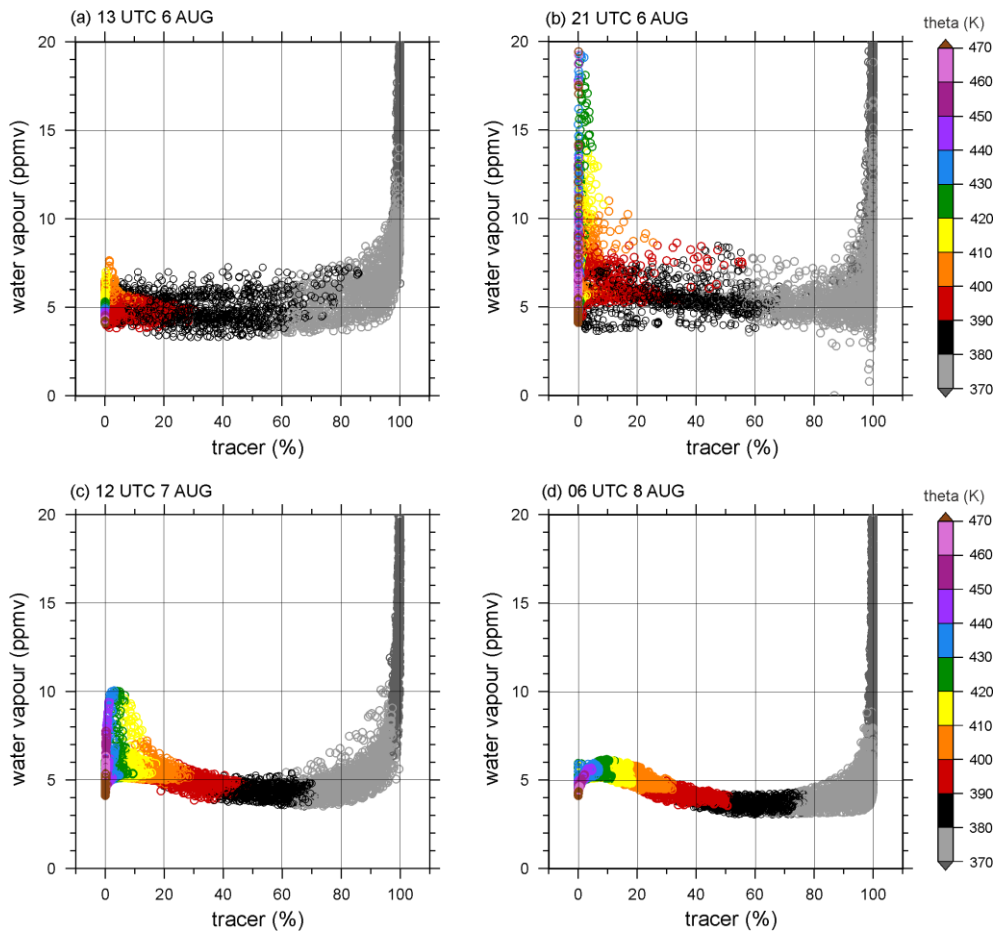
712 **Figure 10.** Hourly evolution of (a) averaged water vapour (line), (b) averaged ice content (solid line, sum of ice, graupel, and snow)
 713 and the precipitating hydrometeor (dashed line, sum of graupel and snow), and (c) averaged temperature (line) and relative humidity
 714 (RH_{ice} , thin line with circle) in the altitudes of 17–18 km (yellow lines) and 18–19 km (blue lines) ASL from 13:00 UTC on 6 August
 715 to 06:00 UTC on 8 August 2017. The four analysis times are marked by open circles on the x-axis. Average and maximum values are
 716 calculated in ML and IL.

717



718

719 **Figure 11.** Vertical profiles of (a) tracer (%), (b) temperature ($^{\circ}\text{C}$), (c) relative humidity (%), mixing ratios of (d) water vapour
 720 (ppmv), (e) ice content (eq. ppmv), and (f) wind speed (m s^{-1}) across the hydration patch along the trajectory at 13:00 UTC (yellow
 721 line), 21:00 UTC (green line) on 6 August, 12:00 UTC on 7 August (blue line), and 06:00 UTC (red line) on 8 August 2017. The
 722 layers of ML and IL are marked by arrows. In (e), the ice content is depicted by solid lines, while the cloud ice are shown by
 723 dashed lines.



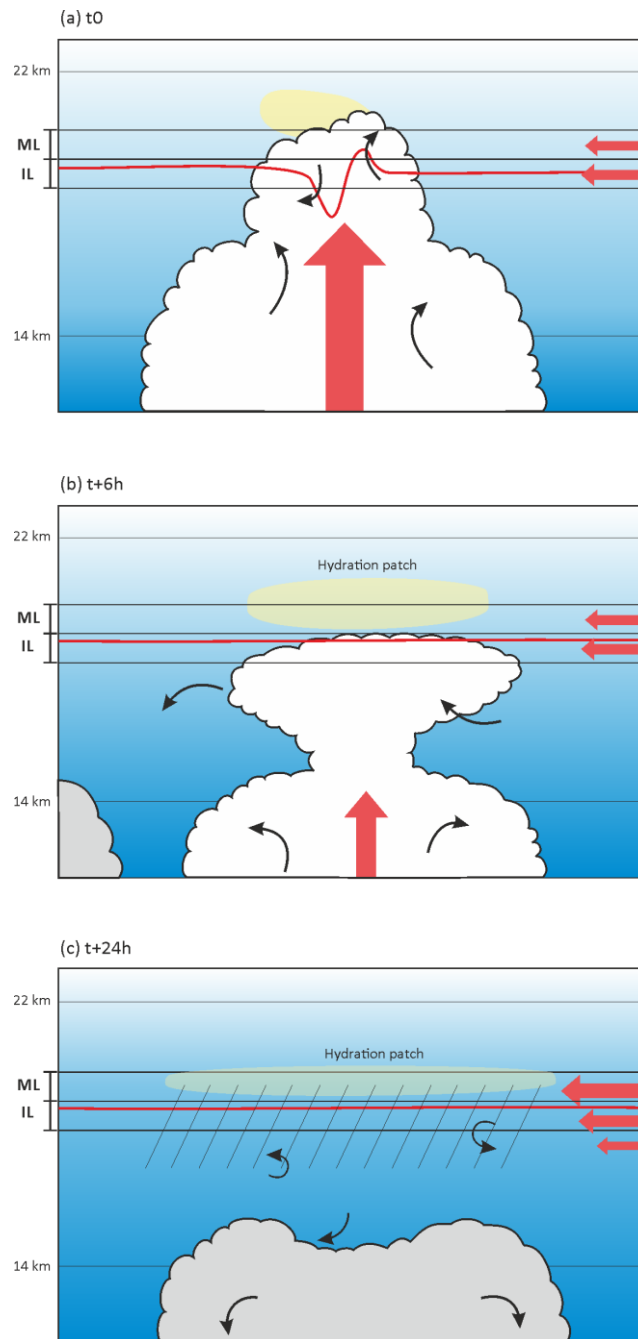
724

725

726

727

Figure 12. Mixing diagram using tropospheric tracer (%) and water vapour (ppmv) across the hydration patch in the altitudes between 14 and 22 km ASL along the trajectory at (a) 13:00 UTC on 6 August, (b) 21:00 UTC on 6 August, (c) 12:00 UTC on 7 August, and (d) 06:00 UTC on 8 August 2017. The potential temperature (K) is shown with colour shading.



728

729

730 **Figure 13.** Schematic illustration summarising the hydration process in the TTL during flight #7 of the StratoClim 2017 field
 731 campaign. (a) Mixing of the overshoots with the stratospheric air, (b) and (c) turbulent mixing of the hydration patch with the
 732 tropospheric air by vertical wind shear. The bottom and top of the TTL, 14 and 22 km, and the moist layer (ML) and ice layer (IL) are
 733 represented by the black solid line, and the 410 K isentropic altitude is represented by the red solid line. The main force in the TTL is
 734 marked by bold red arrows, while the turbulent eddies in/around the developed and weakened overshoots are described by black
 735 arrows. The overreaching water vapour above the cloud top level is indicated by a yellow ellipsoid in (a). The hydration patch is
 736 yellow-encapsulated in (a) and (b), and the layer of dehydration by turbulent diffusion and water vapour deposition followed by ice
 737 sedimentation is hatched in (c). The blue shades illustrate the concentration of tropospheric air, showing the increased tropospheric
 738 air in the TTL by the turbulent mixing in (b) and (c).